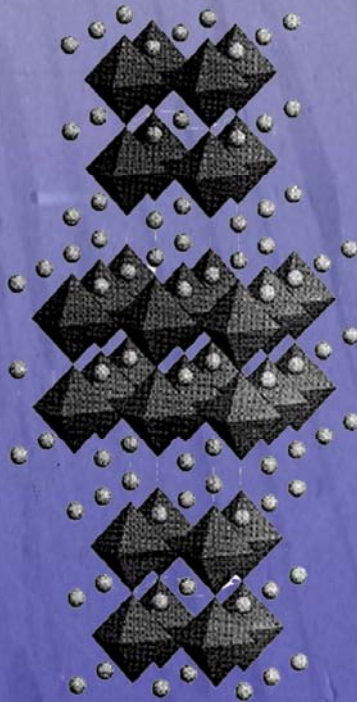


# Crystal growth and characterization of $\text{La}_{1.2}\text{Sr}_{1.8}\text{Mn}_2\text{O}_7$



Wing Kiu Siu  
2004

Van der Waals –Zeeman Instituut

## 0. Abstract

Millimeter sized single crystals of the bilayer manganite  $\text{La}_{1.2}\text{Sr}_{1.8}\text{Mn}_2\text{O}_7$  ( $x=0.4$ ) were grown using the Traveling Floating Zone Technique. The analysis of the single crystals was done with X-ray powder diffraction, Laue X-ray back-reflection, SQUID, polarized optical microscopy and electron microscopy (SEM and EPMA) and the results of this analysis are presented here.

Analysis of the longitudinal and transverse sections with Electron Microscopy showed the presence of two types of composition inhomogeneities in the sample.

Two mechanisms were proposed to understand the formation of this concentration inhomogeneity using proposed schematic phase diagrams.

## 1. Introduction

Since the observation of the Colossal Magnetoresistance (CMR) effect in the manganite perovskites, considerable attention has been given to this family of compounds.

The manganite perovskites are generally represented by the Ruddlesden-Popper (RP) notation  $(\text{R,A})_{n+1}\text{Mn}_n\text{O}_{3n+1}$  (R,A are Lanthanum and Strontium).

In the RP phases the Mn atom is in the centre of an octahedral of oxygen atoms. The Mn and O atoms are arranged in a  $\text{MnO}_2$  plane, similar to the  $\text{CuO}_2$  planes in the High  $T_c$  superconducting cuprates. The  $\text{MnO}_2$  planes are stacked, interleaved with (La,Sr)O planes. The RP phases are categorized by the amount of  $\text{MnO}_2$  planes that are separated by a double rock-salt layer of (La,Sr)O planes. This is schematically represented in figure 1<sup>1</sup>.

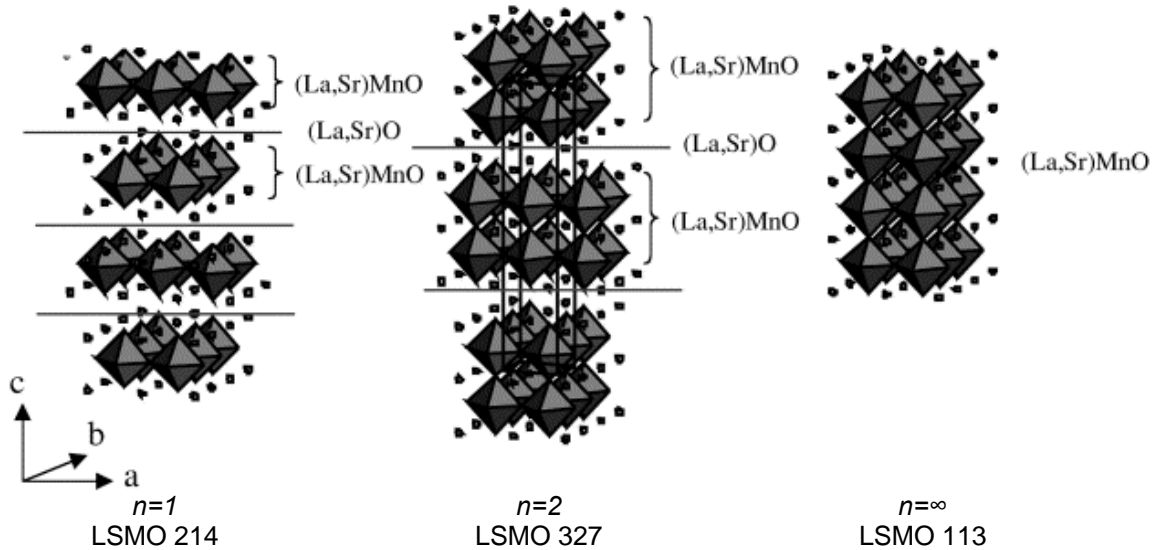


Figure 1: Ruddlesden-Popper phases  $(\text{La,Sr})_{n+1}\text{Mn}_n\text{O}_{3n+1}$  with  $n=1$ ,  $n=2$  and  $n=\infty$ .  $n$  octahedral layers with composition  $(\text{La,Sr})\text{MnO}_3$  are separated by a rock-salt layer of composition  $(\text{La,Sr})\text{O}$ . They form the cleavage planes and are indicated by the solid lines.

As one can see there are structurally two classes in the CMR oxides: the layered samples with one ( $n=1$ ) and two ( $n=2$ ) layers and the three dimensional perovskite samples ( $n=\infty$ ).

The layered samples with one layer, such as  $\text{La}_{1-x}\text{Sr}_{1+x}\text{MnO}_4$  (LSMO 214) and two layers, such as  $\text{La}_{2-2x}\text{Sr}_{1+2x}\text{Mn}_2\text{O}_7$  (LSMO 327) cleave nicely as the rock salt layers are ionic bonded.

The perovskite samples however such as  $\text{La}_{1-x}\text{Sr}_x\text{MnO}_3$  (LSMO 113) may be fractured or scraped in vacuum, as no cleaving plane is present<sup>1</sup>. The perovskite samples are the prototype of the colossal Magnetoresistance materials and many efforts have been made to understand the nature of the CMR effect in this material.

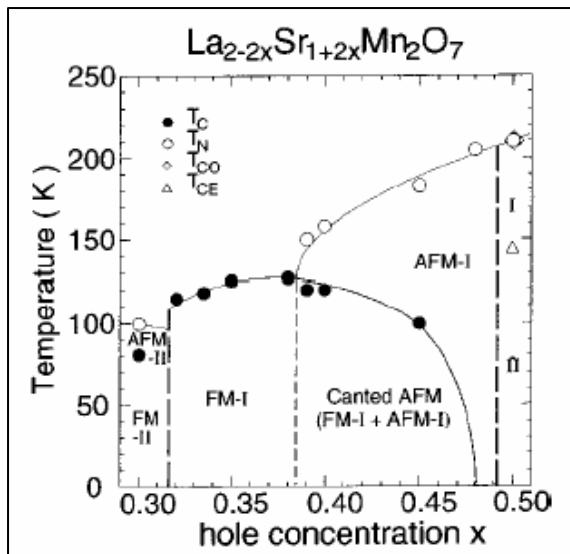
Since Moritomo et al. found an extremely large Magnetoresistance ( $\sim 20\,000\%$ , 129 K,  $H=7\text{T}^2$ ) around the Curie temperature  $T_c$  in a single crystal of  $\text{La}_{1.2}\text{Sr}_{1.8}\text{Mn}_2\text{O}_7$ , many research is done to understand the physics in the bilayer compounds of the RP phases.

One of the efforts was to establish the magnetic and structural phase diagram of  $\text{La}_{2-2x}\text{Sr}_{1+2x}\text{Mn}_2\text{O}_7$  as a function of the doping concentration. Kubota et al. established this phase diagram in the range of  $0.30 \leq x \leq 0.50$  (figure 2a<sup>3</sup>).

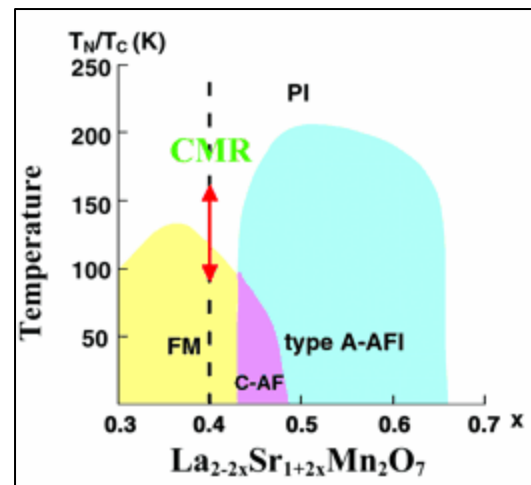
They found that the LSMO 327 exhibits a planar ferromagnetic (FM) structure FM-I (magnetic moments aligned in ab-plane) at low temperatures in the range of  $0.32 \leq x \leq 0.38$ . For high temperatures the compound is in the paramagnetic state.

At  $x \sim 0.39$  a finite canting angle between neighboring layers starts appearing and reaches  $180^\circ$  for  $x \geq 0.48$  (AFM-I e.g A-type AFM). For  $x=0.30$  they found that the magnetic moments were aligned parallel to the c-axis (FM-II, indicating a phase boundary between  $x=0.30$  and 0.32). At  $x=0.50$  the magnetic structure exhibits complicated temperature dependence due to charge ordering<sup>4</sup>.

Chuang et al. however presented a slightly different phase diagram, which was extracted from Ling et al.<sup>5</sup>. This phase diagram (figure 2b) shows a simpler picture for the  $x=0.4$  doping concentration, with only a paramagnetic-ferromagnetic transition.



2a.



2b.

Figure 2: magnetic phase diagram of the layered  $\text{La}_{2-2x}\text{Sr}_{1+2x}\text{Mn}_2\text{O}_7$  by a) Kubota and b) Ling et al.

Although the magnetic and structural phase diagram is complicated, the structure of LSMO 327 is fairly simple. There is only a single tetragonal ( $I4/mmm$ ) phase (fig 3a.) in the entire hole concentration ( $0.30 \leq x \leq 1.0$ ) and temperature ranges ( $T \leq 400\text{K}$ ). This simplicity is probably due to the layered structure, which absorbs the changes in the Mn-O bond lengths and the average ionic radius of La and Sr ions when the hole concentration is changed<sup>4</sup>.

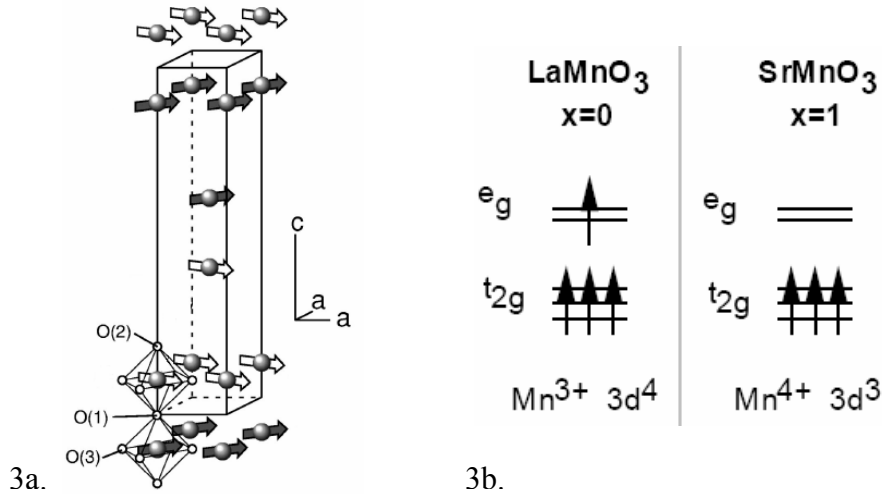


Figure 3a: schematic representation of the magnetic spin arrangement on Mn ions in the  $I4/mmm$  tetragonal cell of  $\text{La}_{1.2}\text{Sr}_{1.8}\text{Mn}_2\text{O}_7$ . Each Mn atom is surrounded by an  $\text{O}_6$  octahedron. The unit cell parameters are  $a=b=3.87 \text{ \AA}$  and  $c=20.1 \text{ \AA}$   
 Figure 3b: The  $\text{Mn}^{3+}$  and  $\text{Mn}^{4+}$  ions.

Changing the hole concentration by replacing La atoms by Sr atoms will affect the charge on the Mn atom. This is illustrated in figure 4<sup>6</sup>. A compound with  $x=0$  (e.g no Sr atoms) will have a  $\text{Mn}^{3+} 3d^4$  arrangement. Increasing the Sr concentration will add more holes to the compound, increasing the  $\text{Mn}^{4+} 3d^3$  concentration. The physics of the manganites will change drastically by the addition of more  $e_g$  conduction electrons. One of the exciting developments of this doping in the manganite perovskites was the discovery of the CMR effect.

#### *Colossal Magnetoresistance (CMR)*

The CMR effect is the very large change in conductivity (typically orders of magnitude) when a magnetic field is applied slightly above the sample's  $T_c$ . This change in conductivity is typically accompanied by a ferromagnetic-paramagnetic transition. This change can also be obtained by changing the temperature across the critical temperature  $T_c$  and thus inducing the ferromagnetic-paramagnetic transition.

This behavior is summarized in figure 4<sup>1</sup>, which shows the resistivity and magnetization as a function of temperature for the layered CMR oxide  $\text{La}_{2-2x}\text{Sr}_{1+2x}\text{Mn}_2\text{O}_7$  for  $x=0.4$ .

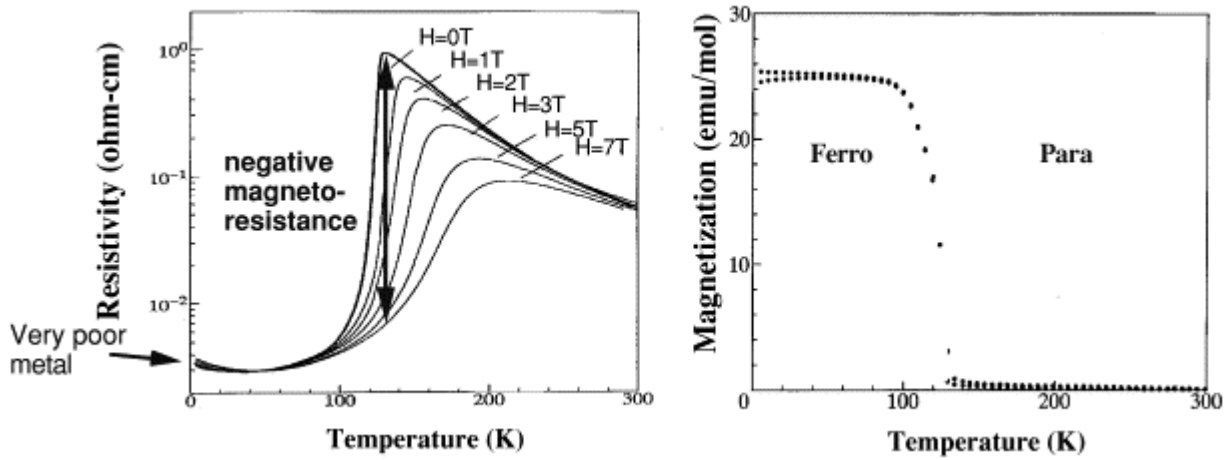


Figure 4: The resistivity vs. temperature and magnetization vs. temperature for the layered CMR oxide  $\text{La}_{2-2x}\text{Sr}_{1+2x}\text{Mn}_2\text{O}_7$  for  $x=0.4$  after Moritomo et al. The resistive and magnetic transitions are at the same or very nearly the same temperatures, indicating a strong coupling of the charge and spin degrees of freedom. This coupling is also obvious from the magnetoresistive behavior shown in panel a.

At high temperature the material is an insulator (increasing resistivity for increasing temperature) while at temperatures below  $T_c = 130$  K the material is a very poor metal. Coincident with the insulating and metallic states are the paramagnetic and ferromagnetic phases of the material.

#### *Double-Exchange model*

Although the origin of the CMR effect as well as the nature of the insulating and poor metallic state are not understood, it is clear that there is a coupling of the charge, spin and lattice degrees of freedom in these compounds.

The charge and spin coupling can be seen in figure 4, where the resistive and magnetic transitions take place at the same or very nearly the same temperature.

The coupling to the lattice (electron-phonon coupling) was recognized in the theoretical work of Millis et al<sup>7</sup>.

The traditional starting point for understanding the CMR effect, Metal-Insulator and PM-FM transitions in the manganites is the Double Exchange model, originally studied by Zener, deGennes and Anderson and Hasegawa in the 1950's and 60's. The DE mechanism says that the hopping probability  $t$  for an  $e_g$  symmetry conduction electron to hop from one site to another depends on the relative angle between the core  $t_{2g}$  spins between the two sites:

$$t = t_0 \cos(\theta/2)$$

where  $t_0$  is the bare hopping probability. This is illustrated in figure 5a. **Fout! Bladwijzer niet gedefinieerd.**<sup>6</sup> If the neighboring spins are ferromagnetically aligned,  $\theta=0$  and there is a maximum hopping probability. If there is an antiferromagnetic ordering, the relative angle is  $180^\circ$  and no hopping probability. A paramagnetic ordering can be approximated by a relative angle of  $90^\circ$  and  $t$  is reduced by  $\cos(\theta/2) = 1/\sqrt{2}$ , 70% of the ferromagnetic

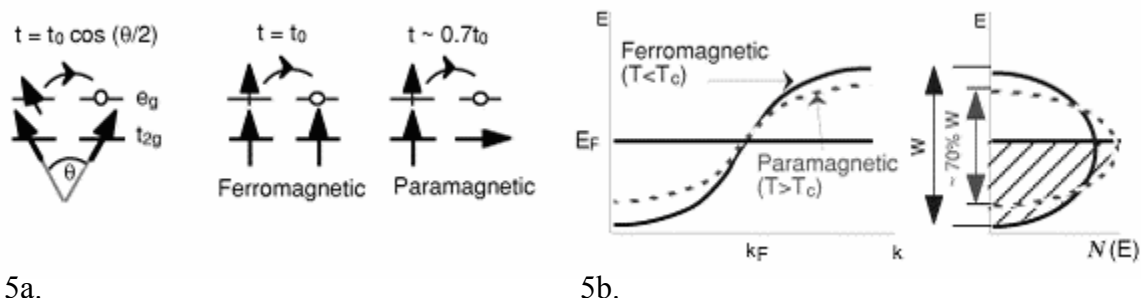


Figure 5a: hopping probability  $t$  depends on the relative angle of the  $t_{2g}$  core spins between two sites. Ferromagnetic state gives a full hopping probability  $t_0$ , while a paramagnetic state has  $0.70 t_0$ .  
 Figure 5b: the hopping probability is related to the bandwidth. The Ferromagnetic state has the greatest bandwidth. The bandwidth of the paramagnetic state is reduced by 30%, predicting an increasing density of states at the Fermi Level.  
 value.

The hopping probability is related to the bandwidth and the ferromagnetic ordering will give the greatest bandwidth. The antiferromagnetic ordering has zero hopping probability and thus zero bandwidth. The bandwidth of the paramagnetic ordering will be 70% of the ferromagnetic bandwidth. Kubo did a more precise calculation of the bandwidth change with temperature and obtained a similar result.

There is thus an energy gain in the  $e_g$  band for the ferromagnetic ordering, competing with the superexchange alignment favoring the antiferromagnetic ordering as well as with the thermal fluctuation which favor disorder. The DE model explains intuitively why a material is a ferromagnetic metal at low temperatures and will become a paramagnetic insulator at high temperatures. When a large magnetic field is applied slightly above  $T_c$ , it will align the core  $t_{2g}$  spins and increase the hopping amplitude for  $e_g$  electrons, thus making the material more metallic.

Although the DE model gives intuitively a nice explanation for the observed transitions and trends in conductivity, it does not explain the magnitude of the CMR effect very well.

The Double Exchange model predicts a 30% decrease in the hopping probability and the bandwidth. These changes in  $t$  and  $W$  will contribute to similar changes in the electron mobility  $\mu$  and the conductivity  $\sigma$  ( $\sigma = ne\mu$ ). As the conductivity change across the FM-PM transition is many orders of magnitude instead of the predicted 30%, additional physics must be necessary to explain the conductivity changes in the manganites.

The DE model also predicts an increase in the density of states at  $E_F$  for the paramagnetic state as the bandwidth is 0.7 of the ferromagnetic state value. This is illustrated in figure 5b. Thus for intermediate doping levels, the density of states at  $E_F$  should slightly increase upon going to the paramagnetic state.

Dessau et al. however found qualitatively different behavior from this and this will be discussed later in this section.

Generally speaking, one can understand the metal-insulator transitions in terms of a change in the number of carriers or in the mobility of the carriers ( $\sigma = ne\mu$ ). In the DE model, the change in conductivity is predominantly explained by a reduction of the mobility of the carriers (hopping probability). Another mechanism which can reduce the mobility is the Anderson localization effects due to disorder, for instance the disorder of the  $t_{2g}$  core spins.

Neither of the two mechanisms should influence the density of states at the Fermi Level. If the reduction in mobility is the dominant mechanism for the metal-insulator transition, a significant density of states is expected, even in the insulating paramagnetic state. Dessau et al. however found experimental data that the change in mobility is not the dominant mechanism.

### The pseudogap

Dessau et al. performed angle-resolved photoemission measurements (ARPES) on the bilayer manganite  $\text{La}_{1.2}\text{Sr}_{1.8}\text{Mn}_2\text{O}_7$  ( $x=0.4$ ,  $d^{3.6}$ )<sup>a</sup>.

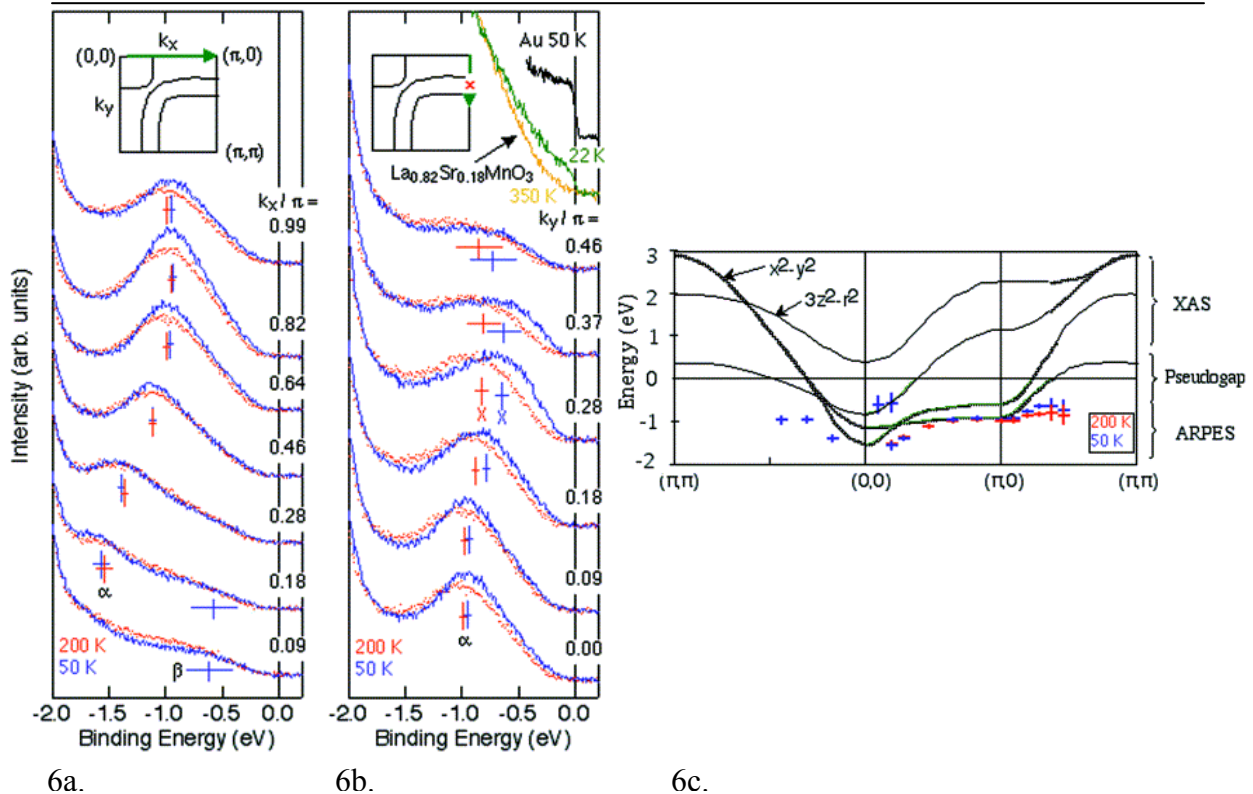


Figure 6: Near- $E_F$  data of  $\text{La}_{1.2}\text{Sr}_{1.8}\text{Mn}_2\text{O}_7$  taken at 200 K (red, paramagnetic state) and 50 K (blue, ferromagnetic state) along the a)  $(0,0)$ - $(\pi,0)$  and b)  $(\pi,0)$ - $(\pi,\pi)$ . Two major features can be distinguished, indicated by  $\alpha$  and  $\beta$ . The upper right hand corner shows  $T$ -dependent angle-integrated data from the three-dimensional compound  $\text{La}_{0.8}\text{Sr}_{0.18}\text{MnO}_3$  as well as from an Au reference.  
Figure 6c: Comparison between experimental dispersion and the LSDA bands (black).

<sup>a</sup> The samples were grown by the floating-zone method and the surfaces of the samples were mirror-like. All samples were measured at the Stanford Synchrotron Radiation Laboratory (SSRL) using a 50mm hemispherical analyzer. The energy resolution was 40 meV FWHM and the  $k$  resolution better than  $\pm 0.05\pi$  in the first Brillouin zone at a photon energy of 22.4 eV. The samples were measured at 50 and 200 K. All 200 K data was taken first, immediately after the sample cleave at 200 K. After all 200 K data were finished the sample was cooled to 50 K.

Figure 6<sup>8</sup> shows the near- $E_F$  data of  $\text{La}_{1.2}\text{Sr}_{1.8}\text{Mn}_2\text{O}_7$  along the  $(0,0)$ - $(\pi,0)$ - $(\pi,\pi)$  symmetry directions at 200 K (Paramagnetic state) and at 50 K (Ferromagnetic state).

In the spectra taken along the  $(0,0)$ - $(\pi,0)$  direction (figure 6a), one can see two major features, which are labeled  $\alpha$  and  $\beta$ . The strongest feature  $\alpha$  is first visible at  $0.18\pi$  and continues to disperse toward  $E_F$  as the spectra progress toward  $(\pi,0)$ . A weak feature visible at  $-0.6$  eV is labeled  $\beta$ .

In the spectra taken along the  $(\pi,0)$ - $(\pi,\pi)$  line (figure 6b) one can also see the  $\alpha$  and  $\beta$  features. Feature  $\alpha$  continues to disperse toward the Fermi Energy, but never reaches it. Instead the locus of the lowest energy is at  $(\pi, 0.37\pi)$  and at this point it loses intensity. This is more clearly illustrated in ARPES data in two earlier published articles by Dessau et al<sup>9,10</sup>.

The centroids of the two features are plotted as a function of  $k$  in figure 6c, which also include the  $e_{g\uparrow}$  bands from their LSDA (Local Spin Density Approximation) band structure calculations.

From their calculations and polarization dependent photoemission experiments they say that  $\alpha$  has primarily  $d_{x^2-y^2}$  symmetry and  $\beta$  primarily  $d_{3z^2-r^2}$  symmetry. As you can see, the energy position of the centroids agree relatively well with the calculations between 0.7 and 1.5 eV. For energy levels closer to  $E_F$  however, the peaks fall off and are suppressed from  $E_F$ . The authors say that this suppression is due to the opening of a *pseudogap* near  $E_F$  and affects the states with  $d_{x^2-y^2}$  symmetry as well as with  $d_{3z^2-r^2}$  symmetry.

In addition, the locations of the experimental minima in binding energy as well as the locations where the spectral weight is rapidly being depleted agree well with the predicted Fermi Surface crossings. However the spectral behavior of these critical  $k$ -points is different from that expected of a real Fermi Surface crossing. The spectral weight reaching the Fermi Energy is close to zero, thus the authors speak of a 'Ghost Fermi Surface'. This is in rough agreement with the FS calculated by the LSDA band theory<sup>10</sup>.

Two important aspects can be seen in the temperature dependence of the near- $E_F$  spectra in figure 7.

The first aspect is that the data only show a very small change in the bandwidth, which is in contradiction with the DE-predicted change.

As was explained earlier, the DE model predicts a 30% decrease in bandwidth when going from the Ferromagnetic to Paramagnetic state. In the data the highest binding energy occupied states was found to be at  $(0.18\pi,0)$  and a binding energy of  $\sim 1.6$  eV. When going to the paramagnetic state, DE predicts that these states should show a significant ( $\sim 30\%$ ) energy shift towards  $E_F$ , thus they should be present around 1.1 eV. Dessau et al. however observed an energy shift of approximately 0.06 eV or a change in  $W$  of just 4%. This implies that a short-range (in-plane) ferromagnetic correlation might still exist above  $T_C$ . This was also found by neutron scattering measurements from the same sample which showed in-plane short-range FM order at temperatures as high as 284 K.

The second aspect is the dramatic temperature dependence near  $k=(\pi, 0.28\pi)$ , in contrast to the small T-dependence of  $k=(\pi, 0.18\pi)$ . The first point corresponds to a predicted FS

crossing and is also the point of closest approach of the centroid to  $E_F$ . The spectra at higher  $T$  are pushed farther away from  $E_F$  and the spectral weight near  $E_F$  is reduced. This behavior represents the opening of the pseudogap centered around  $E_F$  with  $T$ . It is expected then that the states near  $k_F$  are suppressed more heavily than states farther away. Dessau et al. also found this behavior in their data. The term pseudogap was chosen by the authors because the edges of the gap are soft and spectral weight at  $E_F$  is not always completely suppressed.

Spectral weight is also suppressed at temperatures lower than  $T_C$ . The temperature-dependent spectral weight near  $E_F$  is shown in figure 7<sup>10</sup> for the  $k$  value  $(\pi, 0.28, 0)$ . This corresponds to a point on the  $d_{x-y}^2$  Fermi Surface. There is essentially no weight at  $E_F$  above  $T_C$ , but below  $T_C$  the weight starts to increase. Even though the weight is continuously increasing as the temperature is lowered, it still remains a factor 10 less than expected. The pseudogap is active at all temperatures. The pseudogap affects therefore both the Ferromagnetic and Paramagnetic states, although the suppression is more heavily in the Paramagnetic state: the pseudogap is larger above  $T_c$ .

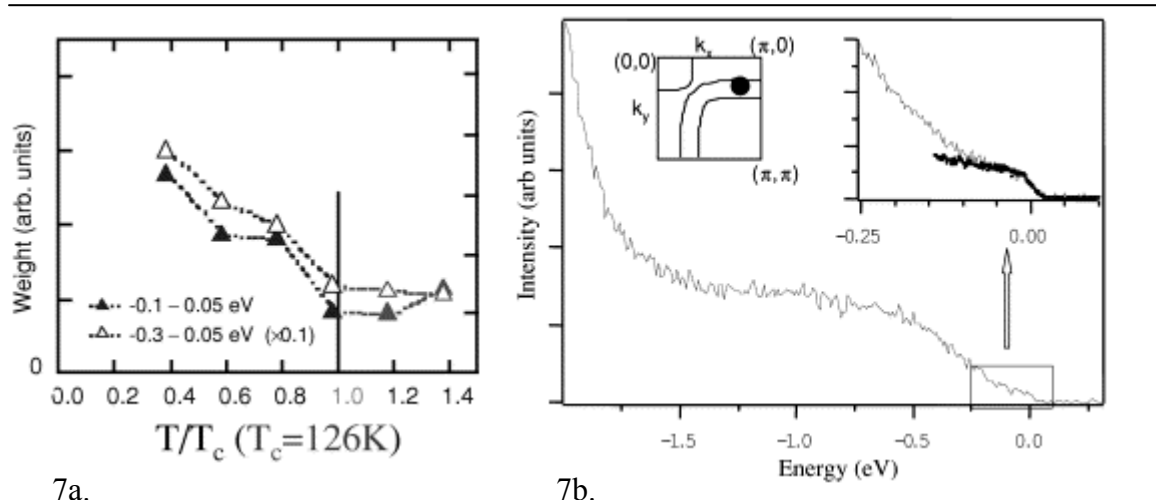


Figure 7a: Temperature-dependence of the spectral weight near  $E_F$  at  $k=(\pi, 0.28, 0)$ ,  $h\nu=22.4$  eV  
 Figure 7b: High-resolution ARPES data near  $E_F$  taken at  $T=20$  K (Ferromagnetic state) showing the Fermi edge cutoff. The  $k$  value is about  $(0.8\pi, 0.28\pi)$  and  $h\nu=50$  eV.  
 A gold spectrum (dark curve) is superimposed to show the small, but finite weight at  $E_F$ .

To resolve the spectral weight at  $E_F$  Dessau et al. took much higher energy and momentum resolution ARPES data at  $T=20$  K (ferromagnetic state). They found a small, but finite spectral weight, occurring very near the  $k$ -space locations where band theory calculations predicts a Fermi Surface crossing<sup>10</sup> (figure 7b).

The ‘ghost’ Fermi Surface, which was termed this way because of the little spectral weight, does contain the expected number of carriers. This was also confirmed by recent Hall measurements. The authors therefore argue that there are a large number of carriers ( $x=0.4$ ), but that each of these carriers is heavily dressed by a correlation effect such that it has very little spectral weight remaining at  $E_F$ .

As the temperature dependence of the pseudogap correspond very well with the observed resistive trends, the authors say that the pseudogap should be considered a key

mechanism cooperating with double-exchange to produce the metal-insulator transition and the CMR effect.

### *Interpretation pseudogap*

A number of possible origins for the pseudogap have been formulated by the authors, such as the Jahn-Teller effect, strong electron-boson coupling, polaronic or bipolaronic effects, phase separation, a coulomb gap, strong on-site correlations and charge/orbital ordering. Whatever the effect is, it should cooperate with and strengthen the Double-Exchange effect, to explain the Metal-Insulator and magnetic transition happening at the same temperature.

The authors later published an article<sup>5</sup> which explained the origin of the pseudogap in terms of Fermi Surface nesting instabilities and the production of nanoscale fluctuating charge/orbital modulations, cooperating with Jahn-Teller distortions.

Some results and their conclusion of this article will be discussed here.

The authors used high-resolution ARPES (Advanced Light Source at the Lawrence Berkeley National Laboratory) to analyze the details of the Fermi Surface and the  $k$ -dependent electronic structure. In figure 9<sup>5</sup> their low-temperature ( $T=20$  K) ARPES data of  $\text{La}_{1.2}\text{Sr}_{1.8}\text{Mn}_2\text{O}_7$  is shown.

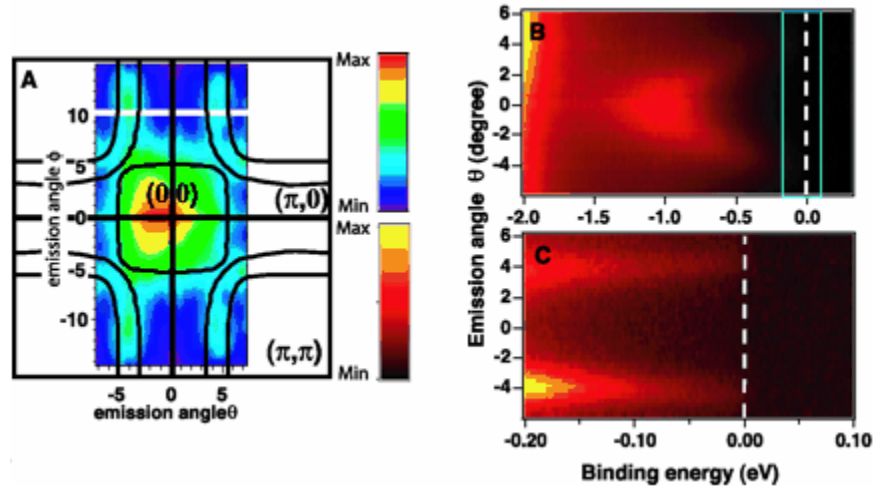


Figure 8a: Low-temperature ( $T=20$ K) ARPES data of  $\text{La}_{1.2}\text{Sr}_{1.8}\text{Mn}_2\text{O}_7$ . The integrated spectral weight near  $E_F$  over much of the first Brillouin zone and the calculated LSDA Fermi Surface (black lines). Data has been reflected about the  $(0,0)-(\pi,0)$  line based on symmetry arguments.

Figure 8b: Binding Energy vs emission angle  $\theta$  image plot from an angular slice at  $(0, 0.7\pi)$  (see white line in figure a).

Figure 8c: Near  $E_F$  blow up of data from b), see the blue box.

As one can see, there is a good agreement between the experimental image plot and the theoretical Fermi Surface in figure 8a. The theoretical FS consists mainly of two parts, one small electron pocket centered around  $(0,0)$  with mainly  $d_{3z^2-r^2}$  character and two concentric large hole pockets centered around the zone corners  $(\pm\pi, \pm\pi)$  with mainly  $d_{x^2-y^2}$  character.

The higher intensity around (0,0) corresponds to the electron hole pocket, although its intensity is enhanced by the out-of-plane photon polarization. The small asymmetry along the (0,0)-( $\pi$ ,0) line is also probably due to this polarization effect.

The four L-shaped loci around the corners correspond to portions of the hole pockets, but where the theory predicts a splitting of the two hole-like pieces, this is not observed in the experimental FS. In theory this splitting is due to the coupling between two MnO<sub>2</sub> planes per unit cell, but probably due to strong in-plane correlation effects, this theoretical splitting is reduced below detectable limits.

In figure 8b the energy versus momentum  $k$  distribution relation is shown. The angular slice is taken at the 10°  $\phi$  angle and is indicated by the white line in figure 8a. There is clearly a dispersive feature of roughly parabolic shape with maximum spectral weight around binding energy 1 eV and  $\theta=0^\circ$ . As this peak disperses toward  $E_F$  it loses spectral weight until no longer visible below 0.3 eV. In figure 8c however the spectra are blown up and the color rescaled and the spectral weight does continue all the way to  $E_F$ , although dropping drastically. It is this very low weight that is responsible for the FS plot in figure 8a.

The origin of the pseudogap can be found in the FS topology in figure 8a. The hole-like portions are very straight (more than expected by the LSDA calculations, especially near the corners of the hole pockets). These straight parallel segments indicate that the physics of these compounds can be considered quasi-1D. These straight FS segments are in addition also prone to (and originate from) nesting instabilities.

A large portion of the FS is connected in  $k$  space to another by the reciprocal lattice vector  $q$ . This can schematically be seen in the following way (figure 9a<sup>5</sup>), the main band hybridizes with an Umklapp band shifted by an amount of  $G$  in  $k$  space. This hybridization will open up a gap of  $2\Delta$ , which lowers the electronic energy of the system. The authors observed a heavy nesting that will gap large portions of the FS, gaining more energy and thus making a distortion more likely. The fact that the entire FS can be

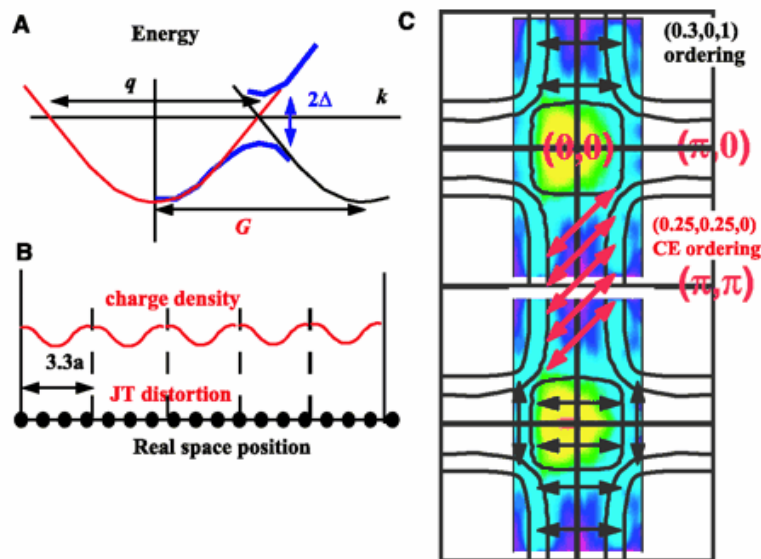


Figure 9a: Schematic plot for density wave formation in  $k$  space

Figure 9b: density wave formation in *real* space with a lattice constant of 3.3  $a$

Figure 9c: Overlay of experimental FS topology with CE-type ordering vectors (red) and orbital stripe ordering (black)

affected by these vectors (figure 9c) means that there will be no ungapped portions remaining, consistent with the insulating state above  $T_C$ .

The  $q$  vector that connects the straight FS segments is probably  $(\pm 0.3, 0)$  or  $(0, \pm 0.3)$  in units of  $2\pi/a$  (see the black lines in figure 9c). The Charge Density Wave corresponding to this wave vector would have a modulation period of  $1/0.3$  or  $3.3$  lattice constants in real space. This incommensurate CDW is illustrated in figure 9b.

The authors also found a cooperative Jahn-Teller style distortion of the  $MnO_6$  octahedra, (period  $3.3a$ ) with the strength of the modulation matching the amplitude of the charge modulation (figure 9b). The coupling of the J-T distortion with the CDW would explain more details of the ARPES data. The CDW can on itself not account for the energy range ( $\sim 1\text{eV}$ ) around  $E_F$  in which the pseudogap depletes the spectral weight. Further more, it was found that the edges of the gap are 'soft', where a simple CDW gap would produce sharp edges. The cooperation of the CDW with the Jahn-Teller distortion can explain the large energy scale and the soft edges of the gap. The typical energy scale of the J-T distortion is near  $1\text{ eV}$  and x-ray results showed that the J-T distortion varies in space, meaning that the resulting gap will have various energy scales and so the gap edge will be soft.

An additional type of weak superlattice reflection was observed in the paramagnetic state in the x-ray scattering experiments on these crystals. They found a so-called CE ordering, with a wave vector  $q_{CE} = (1/4, 1/4, 0) = (\pi/2a, \pi/2a, 0)$ . This is the combination of antiferromagnetism and charge/orbital orderings and is a real space ordering similar to (but different than) a checker board. The CE vectors are drawn in figure 9c (red arrows). They are slightly shorter than the ideal nesting vector and this means that it can still gap the near Fermi states, although with less efficiency than the  $(0.3, 0, 1)$  vector.

To summarize: Dessau et al. have found experimental evidence for the importance of the pseudogap in the resistivity trends. The pseudogap is effective in either explaining the low-temperature poor conductivity of the high-temperature insulating behavior of these compounds. Before the discovery of the pseudogap, the Double Exchange model was considered to be the dominant mechanism in explaining the Metal-Insulator transition.

Experimental evidence suggests that the origin of the pseudogap is the short range charge/orbital density wave enhanced by FS nesting and cooperating with the Jahn-Teller distortion.

## 2. Experimental procedures

In this section the preparation of the  $\text{La}_{1.2}\text{Sr}_{1.8}\text{Mn}_2\text{O}_7$  single crystal and the experimental methods that were used to characterize it are discussed.

### 2.1 From starting compounds to single crystal.

#### *Preparation $\text{La}_{1.2}\text{Sr}_{1.8}\text{Mn}_2\text{O}_7$ powder*

The LSMO powder was prepared by solid-state reaction using  $\text{La}_2\text{O}_3$  (99.99%),  $\text{SrCO}_3$  (99.99%) and  $\text{MnO}_2$  (99.9%). The starting compounds were weighed in the right stoichiometric amounts with a total of 30 g. The compounds were mixed by hand and ball mill for 60 min. until the sample was a homogeneous grey powder to the eye.

The four samples were prepared using different heating procedures. Between each heating session, the sample was grinded with the ball mill for 10 min. The different heating procedures are described in table 1. For the last heating session the powder was pressed into a rod (6000 bar) and sintered, this is denoted by a double bar in the table.

Table 1: Heating procedures for the different samples.

	<b>1</b>	<b>2</b>	<b>3</b>	<b>4</b>
<b>Sample 1</b>	800 °C 12 h	1200 °C 16 h	1400 °C 12 h	1400 °C 12 h
<b>Sample 2</b>	1100 °C 16 h	1300 °C 12 h	1400 °C 24 h	1450 °C 24 h 1500 °C 2 h
<b>Sample 3</b>	1100 °C 24 h	1250 °C 12 h	1400 °C 24 h	1450 °C 24 h 1500 °C 2 h
<b>Sample 4</b>	1100 °C 24 h	1300 °C 24 h	1400 °C 32 h 1400 °C 24 h	1450 °C 24 h 1500 °C 2 h

#### Sample 1

The first sample was prepared using  $\text{MnCO}_3$  instead of  $\text{MnO}_2$  and the total weight of the starting compounds was 15 g.

#### Sample 2

Sample 2 was prepared using  $\text{La}_2\text{O}_3$  that was dried at 1000° C in air for 12 h, since the powder appeared to form  $\text{La}(\text{OH})_3$  (analyzed with X-ray diffraction). Also new batches of  $\text{SrCO}_3$  and  $\text{MnO}_2$  were used.

#### Sample 3

Sample 3 was prepared using  $\text{La}_2\text{O}_3$  that was dried at 120 °C for 12 h because the batch that was dried at 1000 °C looked yellowish to the eye.

#### Sample 4

Sample 4 was prepared using  $\text{La}_2\text{O}_3$  that was dried at 900 °C for 12 h. The drying at 120 °C for 12 h appeared not to suffice as the La content in sample 3 was probably too low.

The Mn content was also probably too low due to evaporation, 0.5% more Mn was added to compensate.

The LSMO rods were analyzed with X-ray diffraction (XRD) to determine the phase. The XRD technique is described in paragraph 2.2.

Subsequently the rods were used to grow single crystals with the traveling floating zone technique.

*Traveling floating zone technique: growth of a single crystal*

Single crystals can be grown using the optical floating zone technique (Crystal Systems Inc, figure 10<sup>11</sup>). The LSMO rod is used as a feed rod and the seed rod is an old LSMO single crystalline piece or a piece of the feed rod. A zone in the feed rod is melted by four halogen lamps (1500 W) focused on the zone by mirrors.

The molten zone is held between the seed and the feed rod by its own surface tension and is moved upwards along the sample by moving the mirror stage. The material will then start to crystallize at the lower end of the zone, on the seed rod. The seed and the feed rod

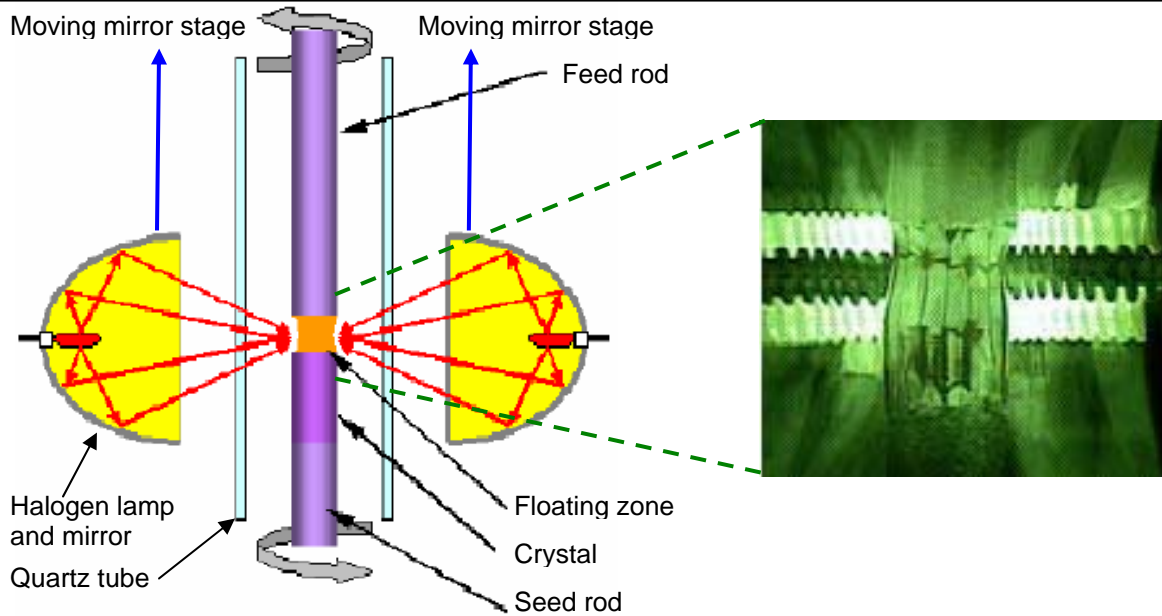


Figure 10: Optical floating zone technique

are counter-rotated to provide an uniform temperature distribution and a homogeneous concentration. The feed and the seed rod are inside a quartz tube in which an O<sub>2</sub>-atmosphere is maintained. The four samples were grown in different conditions:

Table 2: The growth conditions used for the different samples

	Growth rate (mm/h)	Rotation rate (rpm)	O <sub>2</sub> -pressure (atm)
Sample 1	10	20	2
Sample 2	10	20	2
Sample 3	10	30	1.4
Sample 4	15	20	2

The single crystals were analyzed using various techniques:

- *Laue Diffraction* to analyze the quality of the single crystals
- *Superconducting Quantum Interference Device (SQUID)* to determine the magnetization as a function of temperature and the Curie temperature
- *Scanning Electron Microscopy (SEM)* and *Polarized Optical Microscopy* were used to image longitudinal and transversal sections of the rod
- *Electron Probe MicroAnalysis (EPMA)* in Leiden was used to determine the composition of the single crystal

The last three techniques require a flat and smooth crystal surface and the sample was polished before the analysis was performed.

The different techniques are described in paragraph 2.2.

## 2.2 Experimental methods

### X-Ray Diffraction (XRD)

X-Ray Diffraction (Philips Analytical SR 5069) was used to analyze the phase of the polycrystalline rod.

In XRD the powdered sample is irradiated by a monochromatic X-ray beam. The diffracted waves will interfere with each other, producing a diffraction pattern that consists of strong diffraction peaks if the atoms are periodically arranged. The diffracted waves are detected by a detector that can rotate ( $2\theta = 0-90^\circ$ ) and are analyzed using Bragg's law. In this section X-Ray Diffraction will be theoretically discussed.

### Production of X-rays

In X-ray Diffraction the monochromatic X-ray beam is generated in an *X-ray tube*<sup>12</sup> (figure 11a). At one end in the vacuum chamber an electric current runs through a tungsten filament, called the cathode, causing the filament to glow and emit electrons. The electrons are accelerated by a large voltage difference set up between the cathode and the anode. The electrons hit the Cu anode and will eject inner core electrons. Outer shell electrons will fall back in energy to occupy the created vacancies.

The transition of an L-shell electron to the K-shell will create a  $K_\alpha$  X-ray ( $\lambda=1.5418 \text{ \AA}$ ) and the transition from the M-shell to the K-shell will produce a  $K_\beta$  X-ray ( $\lambda=1.5418 \text{ \AA}$ ). The  $K_\alpha$  X-rays have a higher intensity and energy than the  $K_\beta$  X-rays. This difference in energy and wavelength will produce two adjacent peaks in the diffraction pattern; the  $K_\alpha$  and the  $K_\beta$  line.

The process is schematically illustrated in figure 11b<sup>12</sup>. The X-rays then move through a window toward the sample.

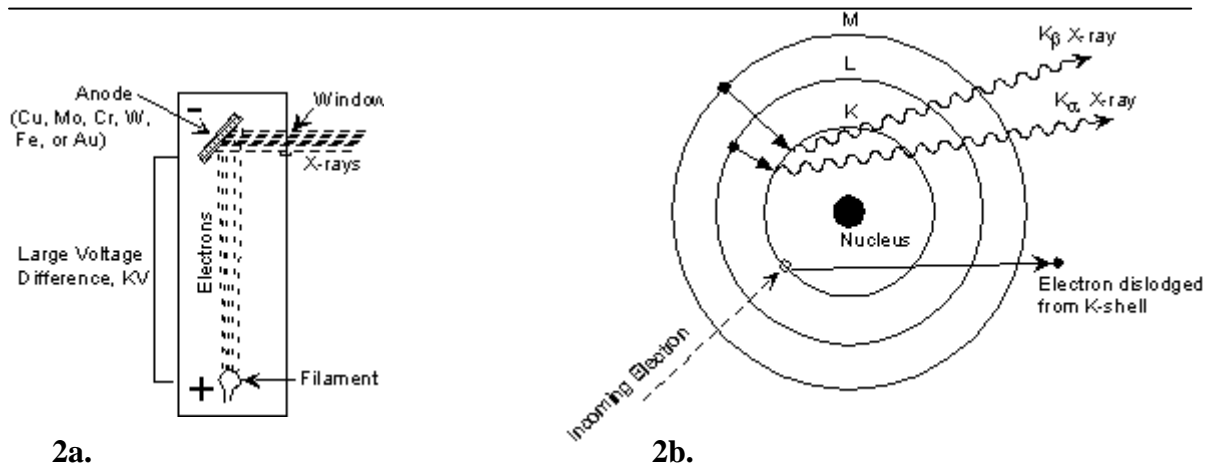


Figure 11a: X-Ray tube.

Figure 11b: Electronic transitions from the M- and L-shell to the K-shell. The  $K_\alpha$  X-rays have a higher intensity and energy than the  $K_\beta$  X-rays.

### Bragg's law

When the incident X-ray beam hits the sample, it will primarily be diffracted by the electrons in the atoms. The scattering is an elastic process and the wavelength of the X-

rays remains unchanged. The scattered X-rays therefore carry information about the electron distribution. As the X-ray beam consists of several waves, the diffracted waves will interfere constructive or destructive with each other depending on the atom's geometry. Ray 2 travels a distance  $2a$  longer in the sample than ray 1. This is schematically illustrated in figure 12. The two waves will interfere constructively and produce a diffraction peak if Bragg's law is satisfied:

$$n\lambda = 2d \sin\theta \quad (1)$$

Where  $\lambda$  is the wavelength of the x-ray beam and  $\theta$  is the scattering angle.

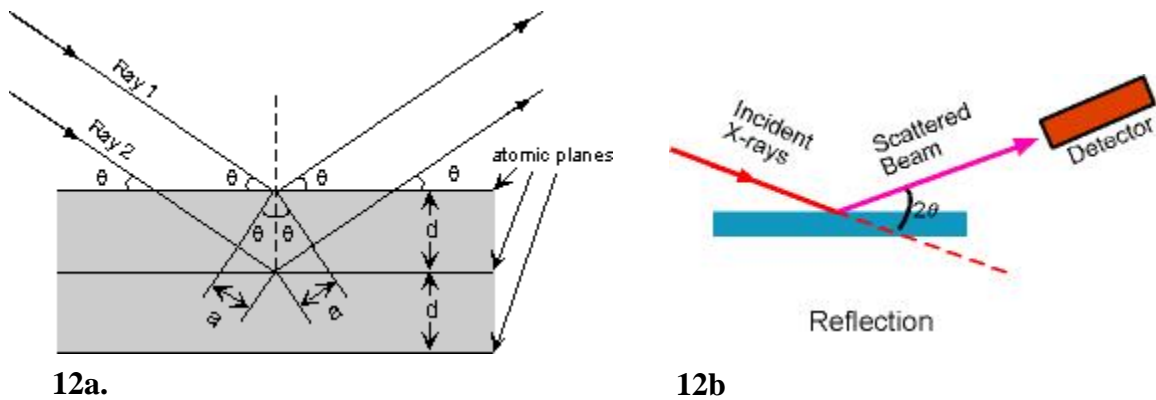


Figure 12a: Bragg's law  
Figure 12b: Schematic XRD setup

In theory one can determine the lattice parameters by varying the scattering angle. This is however a time-consuming method and in practice one uses powder diffraction.

### Powder Diffraction<sup>13</sup>

A single crystal will diffract a monochromatic X-ray beam only in one or two directions (figure 13a<sup>14</sup>). In a powdered sample however the hundreds of crystal domains are randomly orientated, thus the diffracted waves will form continuous cones corresponding to the different d-spacings in the sample (figure 13b<sup>14</sup>).

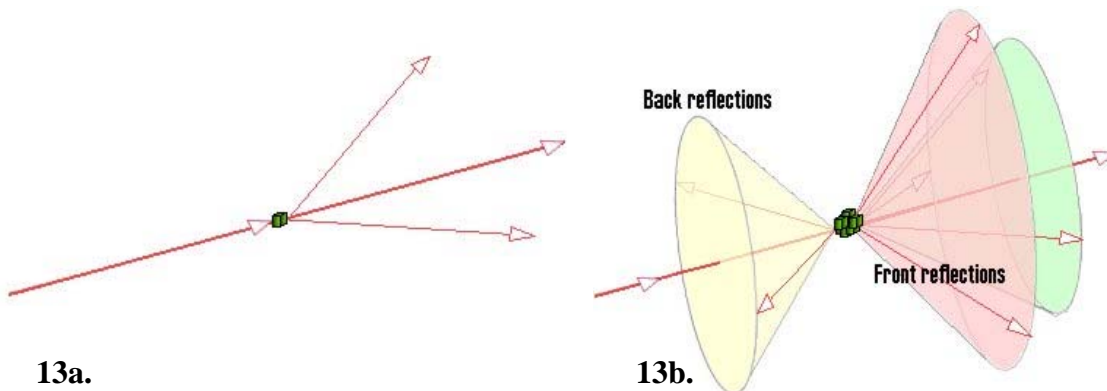


Figure 13a: Scattering by a single crystal  
Figure 13b: Scattering by a powdered sample. The hundreds of crystal domains will scatter the X-rays in a continuous cone, corresponding to different d-spacings in the sample.

A 1D pattern can be recorded by scanning from 0 to 90°. As the crystalline domains are randomly orientated, one can assume that by scanning from 0 to 90° all the angles where diffraction occurs will be found. A schematic setup is shown in figure 3b<sup>13</sup>. The positions and intensities of the peaks can then be used to determine the structure of the sample.

### Laue Diffraction<sup>15,16,17</sup>

Laue Diffraction was used to analyze the quality of the single crystal. In single crystals the atoms are arranged in a regular periodic order, single crystals will scatter incident radiation into a periodic pattern. This phenomenon is made use of in Laue Diffraction. In Laue Diffraction a single crystal is irradiated with white radiation (polychromatic X-ray beam). The diffracted waves will produce spots on a photographic film. The position of the spots is determined by Bragg's law (1). As the atomic spacing  $d$  and the incident angle  $\theta$  of beam is fixed, the only variables are the order  $n$  and wavelength  $\lambda$ . Each order will select a wavelength that will satisfy Bragg's law with fixed  $d$  and  $\theta$ . Each reflection therefore corresponds to a certain order and wavelength. The Laue photograph is therefore just a projection of the planes of the crystal. The Laue diffraction method can also be used to analyze the crystal's quality from the size and shape of the spots. If the crystal is a little bent or twisted the spots will become distorted and smeared out.

A schematic Back-reflection Laue Diffraction setup is shown in figure 14.

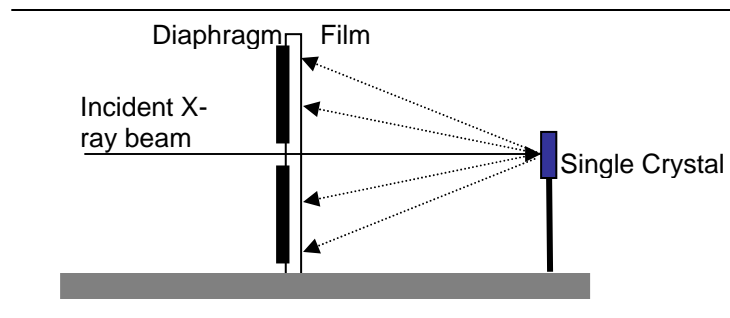


Figure 14: Back-scattered Laue Diffraction

### Polarized Optical Microscopy<sup>18</sup>

Polarized Optical Microscopy (Zeiss axioplan 2) was used to image the longitudinal and transversal sections of the single crystal rod.

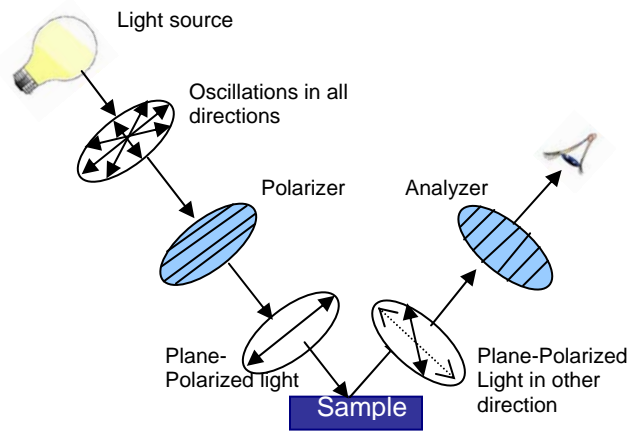
In polarized microscopy one can visualize the anisotropic character of the crystal using a polarizer and an analyzer. In a polarizer the oscillations in all directions in the light beam are polarized to lie in one plane.

The polarizer is placed in the light beam before the sample and the analyzer (e.g a second polarizer) is placed between the objective aperture and the observation tubes or camera port. The polarizer and analyzer are placed with right angles to each other (crossed polarizers) and no light can pass through the analyzer.

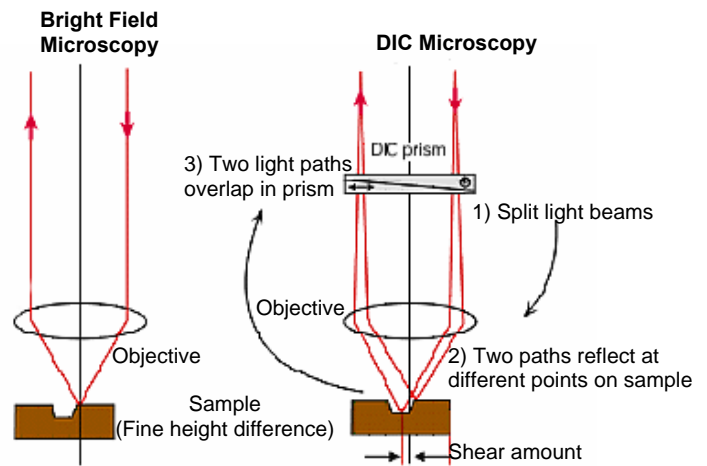
If the polarized light impinges on the sample surface, the polarization of the light will change due to the anisotropic and birefringent character of the material. The material will therefore produce an image contrast (figure 15a).

Differences in the crystallographic axes will change the optical properties of the material. Changes in phase, composition and orientation of the crystallographic axes can therefore be imaged using polarized microscopy.

In addition to polarized microscopy another method can be used to image the crystal surface.



15a.



15b

Figure 15a: Polarized Microscopy

Figure 15b: Differential Interference Microscopy

### *Differential Interference Contrast (DIC)<sup>19</sup>*

In DIC a special crystal prism is placed in the light path, not used in bright field microscopy. In figure 15b the differences between bright field and DIC microscopy are illustrated.

In bright field microscopy the light passes through an objective and is reflected by the sample back through the objective to form an image. In DIC microscopy a special crystal prism is placed in the light path before the objective. The prism splits the light beam into two paths and they are spatially separated by a very small distance, called a 'shear amount'. The two rays are reflected by the sample at two different points separated by the shear amount and travel back through the objective. The two light beams will overlap in the prism and the spatial difference between the points at which the light was reflected result in a phase difference between the two beams. This phase difference results in interference when they overlap in the prism, generating contrast equivalent to the phase difference. If there is no phase difference the image will appear uniform gray.

DIC microscopy can be used to image differences in height and refractive indices. Differences in refractive index will also result in a change in the optical path and phase difference.

## Superconducting Quantum Interference Device (SQUID)

SQUID (Quantum Design MPMS-5S) was used to measure the magnetization of the single crystal as a function of temperature.

SQUID can be used to detect very weak magnetic fields in the order of  $10^{-14}$  T (Earth's magnetic Field is  $0.5 \times 10^{-4}$  T). It makes use of two superconductors separated by two thin insulating layers, forming two *Josephson Junctions* (Figure 16)<sup>20</sup>.

Cooper pairs can tunnel across the Josephson junction. The Cooper pairs can be described by a wave function, similar to a free particle wave function. When no voltage is applied, a current proportional to the phase difference of the wave functions can run across the junction, as Josephson has showed:

$$I_s = I_{\max} \sin(\varphi_1 - \varphi_2) = I_{\max} \sin(\delta) \quad (2)$$

However when a voltage is applied, the current through the junction will oscillate with a characteristic frequency which is proportional to the applied voltage.

$$I = I_{\max} \sin(\delta + 2\pi f t) \quad (3)$$

$$f = \frac{2eV}{h} \quad (4)$$

The sensitivity of the SQUID for measuring magnetic fields depends on *Quantum Interference*<sup>21</sup>. This is the behavior of the tunneling current in the presence of an external magnetic field.

The maximum critical current depends on the magnetic flux that runs through the junction and the current is predicted to depend periodically on the magnetic flux. This is due to the fact that the change in phase across the junction is dependent on the change in magnetic flux.

When one keeps the biasing current constant in the SQUID, the measured voltage will oscillate and one period of voltage variation corresponds to an increase of 1 flux quantum, which is quantized as:

$$\Phi_0 = \frac{2\pi\hbar}{2e} \cong 2.0678 \times 10^{-15} \text{ tesla} \cdot \text{m}^2 \quad (5)$$

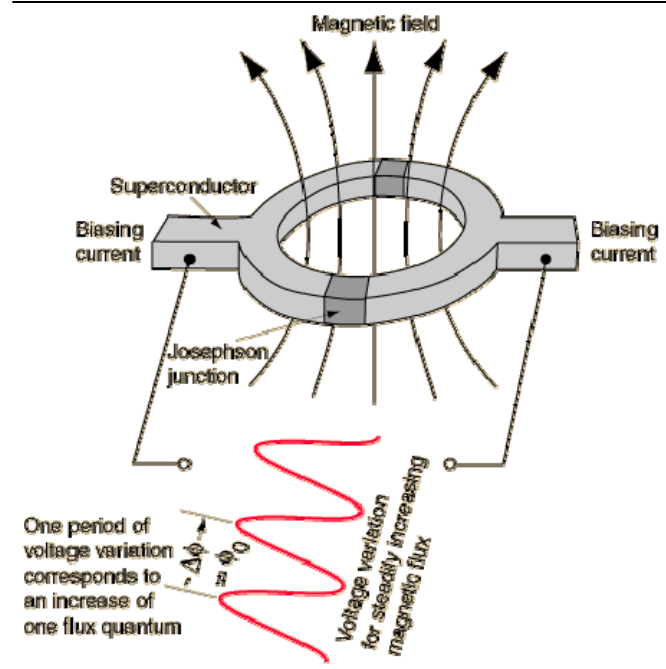


Figure 16: Josephson Junction

## Scanning Electron Microscopy (SEM)

Scanning Electron Microscopy (Jeol JSM-840A) was used to image the longitudinal and transversal sections of the single-crystal rod. The SEM is a microscope that uses electrons instead of light to image samples with a higher resolution than optical microscopes. In figure 17a, a schematic SEM is shown<sup>22,23</sup>.

In the *electron gun*<sup>24</sup> a current is run through a tungsten filament, causing it to heat up and emit electrons. The electrons are then accelerated toward the positive anode, producing a monochromatic electron beam.

The beam is condensed by the first condenser lens and any high-angle electrons will be eliminated by the condenser aperture.

The beam is focused by the second condenser lens, producing a thin, tight coherent beam. A second objective aperture eliminates high-angle electrons.

A set of coils will scan the beam in a grid fashion.

The third objective lens focuses the beam onto the part of the sample which is scanned.

When the electron beam hits the sample, several processes take place<sup>25</sup>, which are illustrated in figure 17b<sup>22</sup>.

*Backscattered Electrons* are produced when an incident electron hits an atom in the sample which is (partially) in its path. The incident electron is then scattered approximately 180 ° back. Heavier atoms will scatter incident electrons more and appear brighter than lighter atoms. This mode is used to image composition differences in the sample.

*Secondary electrons* are produced when the incident electron gives part of its energy to a lower energy electron in the sample (usually a K-shell electron). The electron in the sample-atom will become ionized and leave the atom with a small kinetic energy (5 eV), this electron is called a secondary electron. The incident electron will change path and can ionize several other atoms. This mode can be used to image the topography of the sample, as only secondary electrons that are very near the surface (< 10nm) can leave the sample, due to its low kinetic energy.

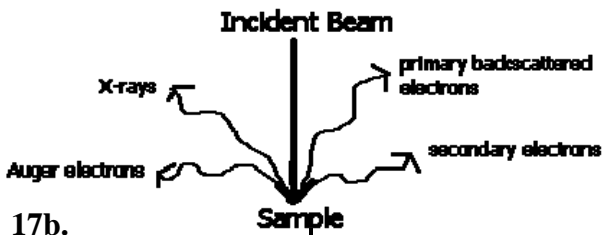
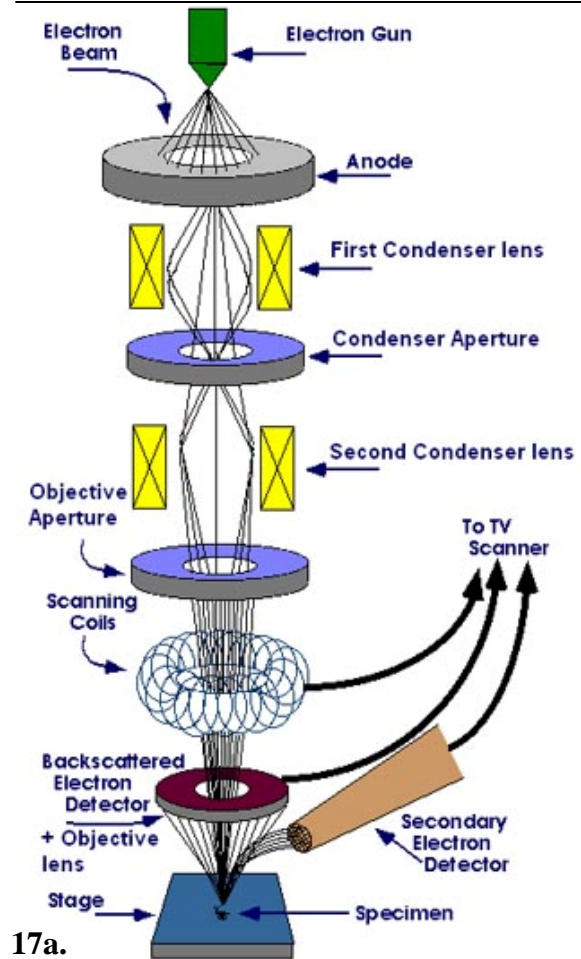


Figure 17a: Schematic SEM setup

Figure 17a: When incident beam hits the sample several processes take place

*Auger electrons*: the production of a secondary electron creates a vacancy, which will be occupied by an electron from a higher energy shell. The energy difference between the two shells is used to ionize an outer, lower energy electron, an Auger electron.

*X-rays* are produced when a higher energy electron falls back to occupy a vacancy in a lower shell, which was created by the production of a secondary electron. As the electron falls back, it will emit its energy as an X-ray. The X-rays have a characteristic energy unique to the element from which it is produced. The X-rays can therefore be used to determine the composition of the sample.

In SEM the Backscattered and the Secondary electron mode is used, giving composition and topographic information.

### **Electron Probe MicroAnalysis (EPMA)**

EPMA was used to determine the composition of the single crystal.

The EPMA has a similar setup to the SEM. The SEM however cannot measure and analyze the X-rays produced by the formation of Auger electrons and the EPMA does have this ability. There are several differences between the SEM and the EPMA setups.

The EPMA uses an electron beam current from 10-200 nA, roughly 1000 times higher than the SEM, to produce more X-rays from the sample and improve the detection limits and accuracy of the analysis.

In order to detect the X-rays, the EPMA is in addition to the backscattered and secondary electron detectors equipped with three to six wave dispersive x-ray spectrometers<sup>26</sup>, which can detect and count the x-rays. The X-rays are analyzed by diffracting the waves by crystals<sup>27</sup>. The chemical composition is determined by comparing the intensity of the X-rays from standards to the intensity of the sample. It should be noted that measuring elements lighter than Oxygen should be done with care.

### 3. Results

In this section, the results of the four different samples will be discussed. Each sample and its results will be discussed separately.

#### Sample 1

In figure 18 the XRD spectrum of the sample after sintering (1450 °C, 12 h) and after growth are shown together with a generated spectrum of  $\text{La}_{1.2}\text{Sr}_{1.8}\text{Mn}_2\text{O}_7$ . The spectrum is generated using *CaRIne Crystallography 3.1* and the size of the atoms was not taken into account. The intensities of the peaks are therefore not representative.

The analysis of the experimental spectra was done using measured reference spectra of the XRD analyzing program. The experimental spectra are shown together with the generated spectrum for clarity.

The XRD spectrum after sintering exhibits little peaks and it is therefore hard to draw conclusions regarding the phase.

The spectrum after sintering was compared with reference spectra of  $\text{La}_{1.5}\text{Sr}_{0.5}\text{MnO}_4$  (214),  $\text{La}_{0.65}\text{Sr}_{0.35}\text{MnO}_3$  (113) and  $\text{La}_{2.0}\text{Sr}_{1.0}\text{Mn}_2\text{O}_7$  (327). The prominent peaks in the spectrum can both be ascribed to the LSMO 113 and 327 phases. The peak at  $2\theta = 40^\circ$  (pink) however can only be ascribed to the 113 phase, suggesting that this is the major phase. The minor peaks at  $2\theta = 43^\circ$  and  $2\theta = 45.5^\circ$  can only be ascribed to the 327 phase (blue), thus there is a minor fraction of the desired phase present.

XRDs were taken from the  $\text{La}_2\text{O}_3$  and  $\text{SrCO}_3$  batches to control the quality of the starting compounds. It appeared that  $\text{La}_2\text{O}_3$  had formed  $\text{La}(\text{OH})_3$  complexes. The La-ratio in the sample was therefore too low, decreasing the (La,Sr) to Mn ratio below 3:2. As a result the LSMO 113 phase was formed with a minor fraction of the LSMO 327 phase.

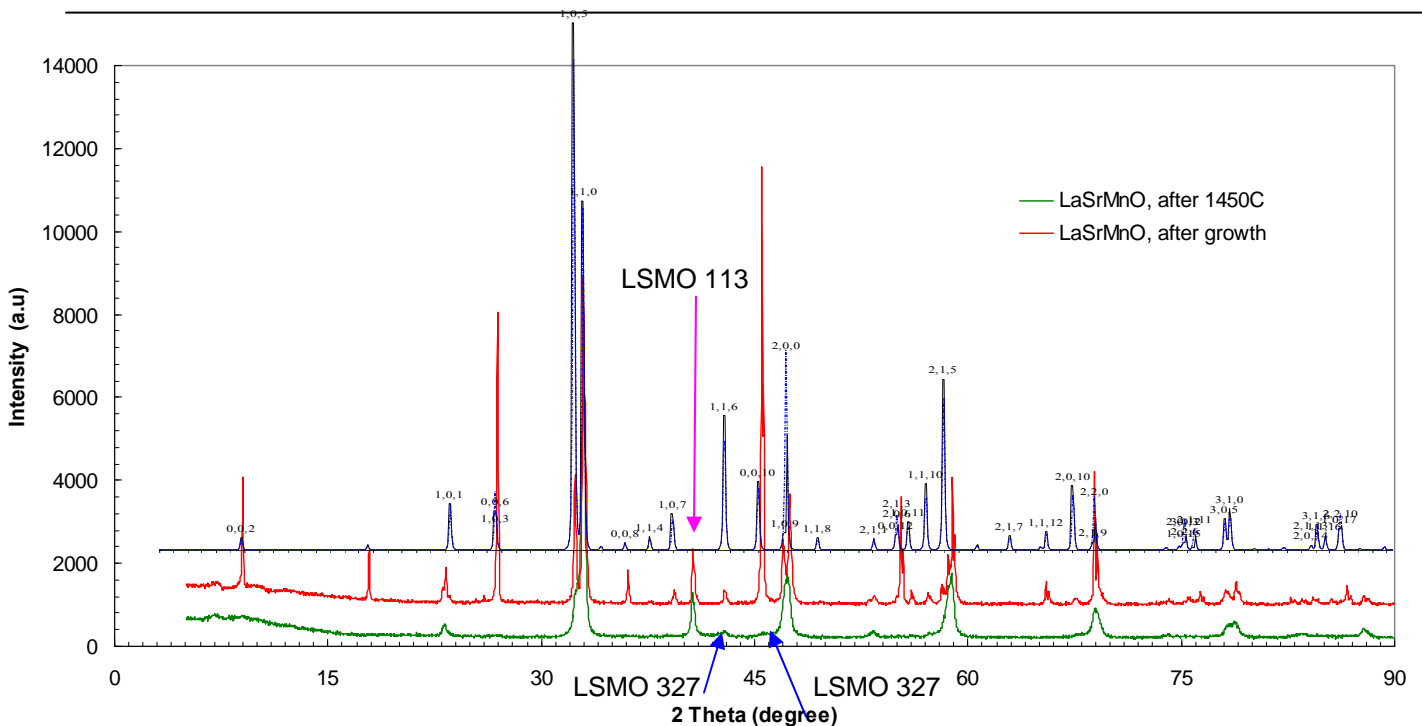


Figure 18: XRD spectrum of the LSMO powder and the LSMO after growth.

After the crystal growth the rod was polycrystalline, because many grain boundaries were visible under the microscope. The crystal growth also indicated that the sample was a 2 phase system, since the melting of the feed rod was not uniform. Little parts of the feed rod already melted outside the hot zone of the furnace, indicating the inhomogeneity of the sample.

The XRD spectrum of the sample after growth is shown in figure 18 and is compared to the generated spectrum of  $\text{La}_{1.2}\text{Sr}_{1.8}\text{Mn}_2\text{O}_7$ . The resemblance between the two spectra is clear. One peak can however only be ascribed to the LSMO 113 phase and is indicated with the pink arrow. Two peaks in the spectrum can only be ascribed to the LSMO 327 phase and are indicated with blue arrows. The polycrystalline rod is therefore a mixture of the LSMO 113 and the 327 phase.

The 0,0,c peaks of the sample after growth are large compared to the reference peaks of the analysizin program. This is due to the preferential orientation of the crystals; the crystallites have a plate-like shape with the c-axis perpendicular to the plane. When preparing the powdered sample for the XRD the ab-planes tend to orientate parallel to each other.

## Sample 2

### X-ray Diffraction

XRDs were taken of the sample before sintering (1400°C, 24h) and after crystal growth. Both spectra are compared to the generated spectrum of  $\text{La}_{1.2}\text{Sr}_{1.8}\text{Mn}_2\text{O}_7$  in figure 19.

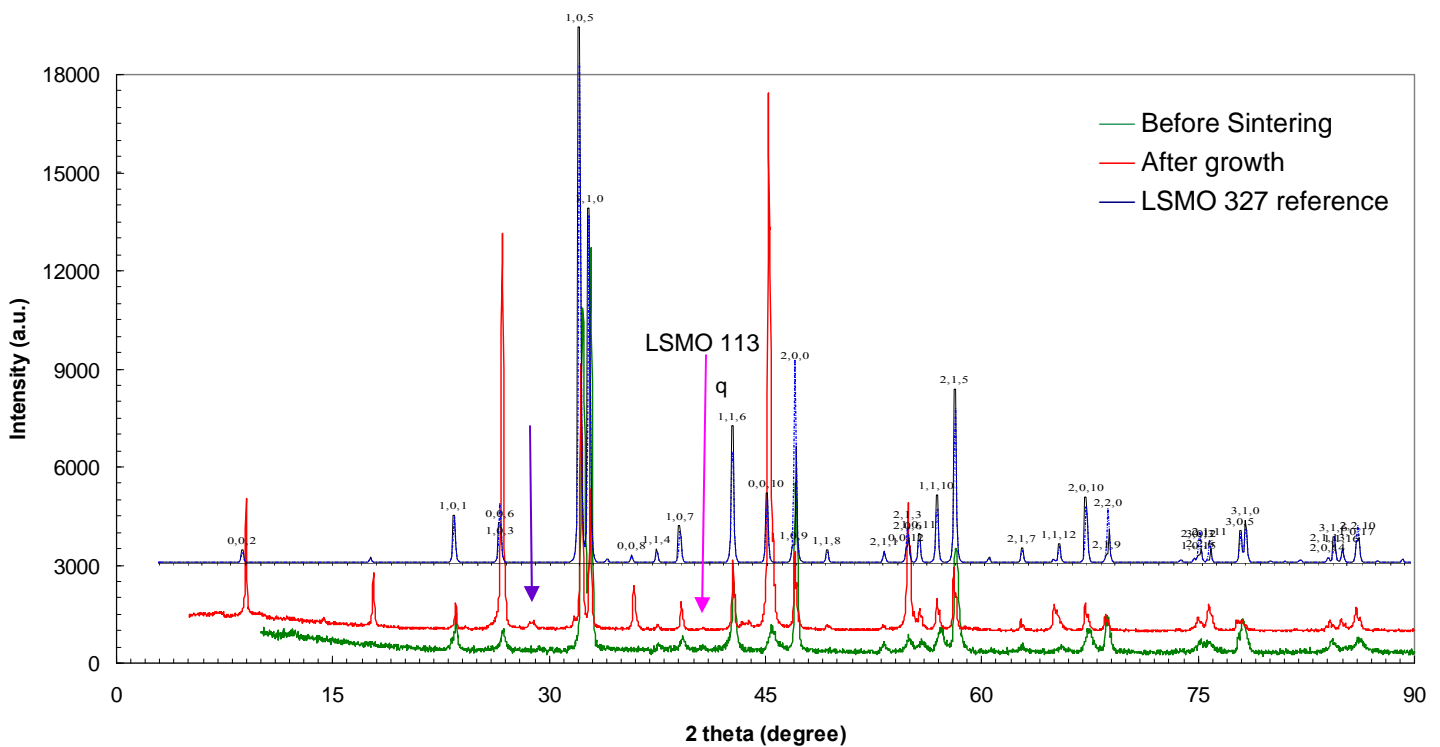


Figure 19: XRD spectrum of the LSMO powder and the LSMO after growth.

The XRD before sintering shows a close resemblance to the reference spectrum, indicating the sample is the desired LSMO 327 phase. One minor peak however shows the presence of a second minority phase (LSMO 113) and is indicated with the pink arrow.

After growth the sample possessed millimeter scale domains of single-crystalline material. The growth direction was parallel to the ab planes and perpendicular to the c-axis (20.2 Å). The crystal was cleaved along a grain boundary, parallel to the ab planes. The XRD spectrum of the single crystalline rod indicates the presence of the LSMO 327 phase. The fraction of LSMO 113 phase, which was initially present in the polycrystalline rod, has decreased in the crystal growth process. A second peak at  $2\theta=29^\circ$  (purple arrow), which could not be ascribed to the LSMO 327 phase is however present and indicates the presence of another phase. This phase could not be ascribed to the LSMO 113, 214 and 327 phases and it is unknown what the composition of this phase is.

### Laue Diffraction

In figure 21 the Laue picture from the sample (20 kV, 40 mA, 10 min) and a generated Laue picture of  $\text{La}_{1.2}\text{Sr}_{1.8}\text{Mn}_2\text{O}_7$  are shown.

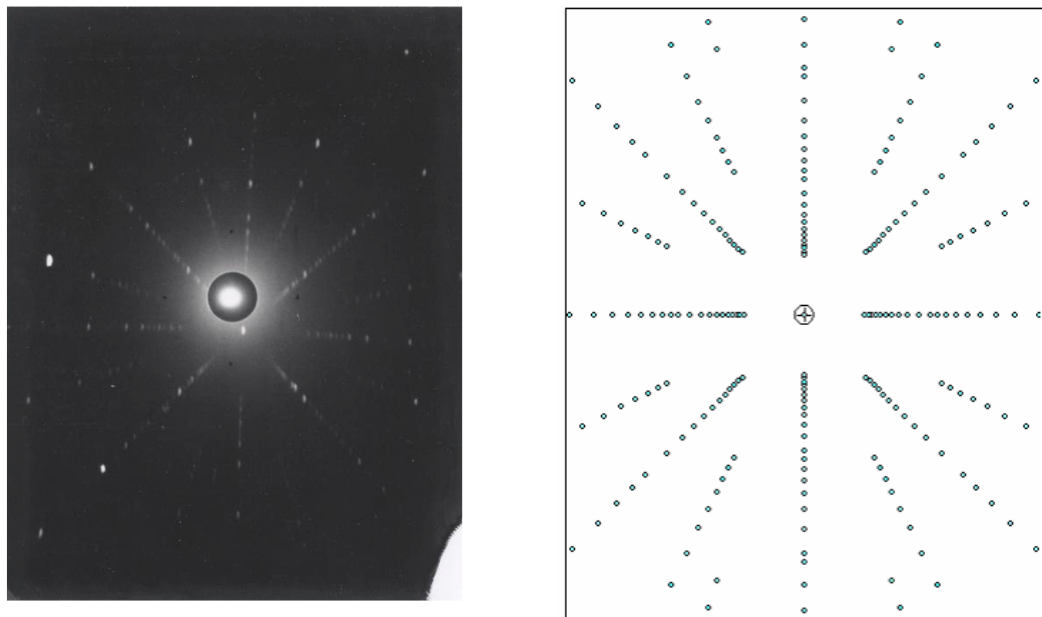


Figure 21: experimental and reference Laue pictures of  $\text{La}_{1.2}\text{Sr}_{1.8}\text{Mn}_2\text{O}_7$

The reference Laue picture is generated by *OrientExpress* using the lattice constants  $a=3.870 \text{ \AA}$ ,  $b=3.870 \text{ \AA}$ ,  $c=20.100 \text{ \AA}$ . <sup>Fout! Bladwijzer niet gedefinieerd.</sup> Thus the size of the atoms is not taken into account.

The experimental and reference Laue pictures show a close resemblance and the sample has the desired crystal structure.

The points in the experimental Laue picture are however a bit elongated, indicating a deviation from the perfect crystal structure. The big spots visible in the left side of the picture are not understood and are not due to defects of the apparatus.

### *Electron Probe MicroAnalysis*

In figure 22 a picture from the longitudinal section (parallel to the ab-planes) of the rod taken in backscattered electron mode is shown. One can clearly see a stripe-like pattern where the stripes are regularly spaced. The crystal has an inhomogeneous composition.

The composition was measured in 3 different areas, the main phase (matrix), the darkest stripe and in a white precipitate (indicated with an arrow). The composition is normalized to the Mn-concentration, which is set to 2.00. The matrix phase has the desired composition

of  $\text{La}_{1.2}\text{Sr}_{1.8}\text{Mn}_2\text{O}_7$ . As was mentioned before, the measured Oxygen concentration should be interpreted with care. The matrix and dark stripes both have the same LSMO 327 structure and only differ in composition. The darker stripes have a lower La-concentration and a higher Sr-concentration, but the composition difference between the two phases is small.

The white precipitates are the LSMO 214 phase, but form only a minor fraction of the sample (<1%).

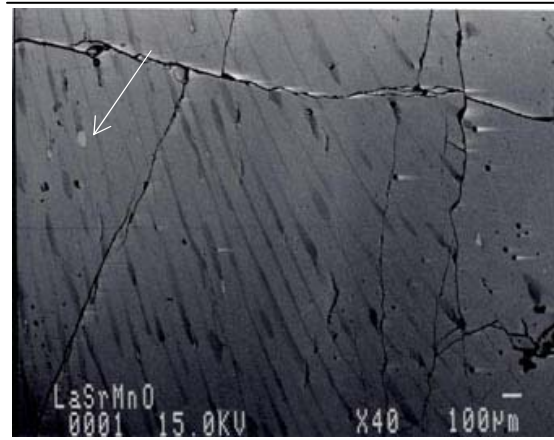


Figure 22: EPMA picture of crystal surface showing composition differences

Table 3: Composition analysis of the matrix, dark stripes and white precipitates in the sample

	<b>La</b>	<b>Sr</b>	<b>Mn</b>	<b>O</b>	<b>La+Sr</b>
Matrix	1.19	1.79	2.00	6.22	2.97
Dark stripes	1.08	1.85	2.00	6.26	2.93
White precipitates	1.27	2.72	2.00	7.05	3.98

### *Annealing*

In order to understand the composition oscillation mechanism within the crystal, we have tried to anneal the crystal in air.

The first annealing took place in 1100 °C for 60 h. The sample was embedded in the acrylic resin, grinded and polished and was imaged using SEM and polarized microscope. The annealed sample still exhibited the stripe-like pattern, indicating the composition differences in the sample.

Another annealing with another crystal piece was carried out in 1400 °C for 50 h and was quenched in air. This annealing also did not result in a homogeneous sample.

## SQUID

A small crystalline piece was used to measure the magnetization as a function of temperature ( $T=5-350\text{K}$ ) to determine the Curie temperature. The M-T diagram is shown in figure 23.

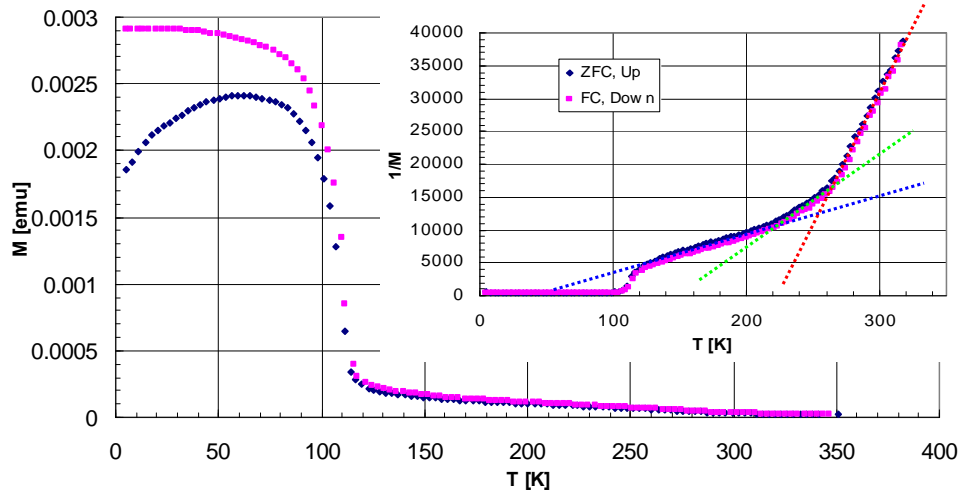


Figure 23: Magnetization as a function of temperature,  $T_c=120\text{ K}$ . Inset shows  $1/M$  as a function of temperature. One can see three different regimes after  $T_c=120\text{ K}$ . Two kink points can be observed at  $220\text{ K}$  and  $270\text{ K}$ .

After Zero-Field Cooling (ZFC) the M-T diagram was recorded while the sample was heated up from  $5\text{ K}$  to  $350\text{ K}$  and then cooled down (Field-Cooling). The applied magnetic field was  $50\text{ Gauss}$ .

The transition at  $T=120\text{ K}$  is probably a ferromagnetic transition and was also measured by S.H Chun et al. ( $T_c=121\text{ K}$ )<sup>28</sup>. The difference between the ZFC and FC diagrams below  $50\text{ K}$  was also mentioned by S.H Chun and may be attributed to a spin glass transition<sup>28</sup>.

In the inset the inverse of the magnetization as a function of temperature is shown. Three different regimes can be observed after the lower transition temperature. Two kinks are present at  $T = 220\text{ K}$  and  $T = 270\text{ K}$ . This behavior was not mentioned by Chun et al. but is mentioned by N.O Moreno<sup>29</sup>. Moreno et al. found one to four additional transitions, depending on the sample. They ascribe these transitions to extrinsic Ruddlesden-Popper phases and not to an intrinsic effect as has been claimed. They could not determine the origin of the extrinsic phases, but conclude that it are RP phases with  $n \geq 3$  since  $n=1$  orders antiferromagnetic. Regarding the distribution of  $T_c^*$  that they found for different samples ( $290-310\text{K}$  and  $260-360\text{ K}$ ) they claim that this could result from the presence of intergrowths with different values of  $n$  and/or hole (Sr) concentration.

The presence of the addition transitions is therefore due to extrinsic phases as can be confirmed with the composition analysis. The composition was not homogeneous and phases with different La/Sr ratio were present.

### Sample 3

#### *X-Ray Diffraction*

The XRD spectrum of the sintered sample (1450 °C 24 h, 1500 °C 2 h) is shown in figure 24 with the  $\text{La}_{2.0}\text{Sr}_{1.0}\text{Mn}_2\text{O}_7$  (green) and  $\text{La}_{0.65}\text{Sr}_{0.35}\text{MnO}_3$  (yellow) reference spectra.

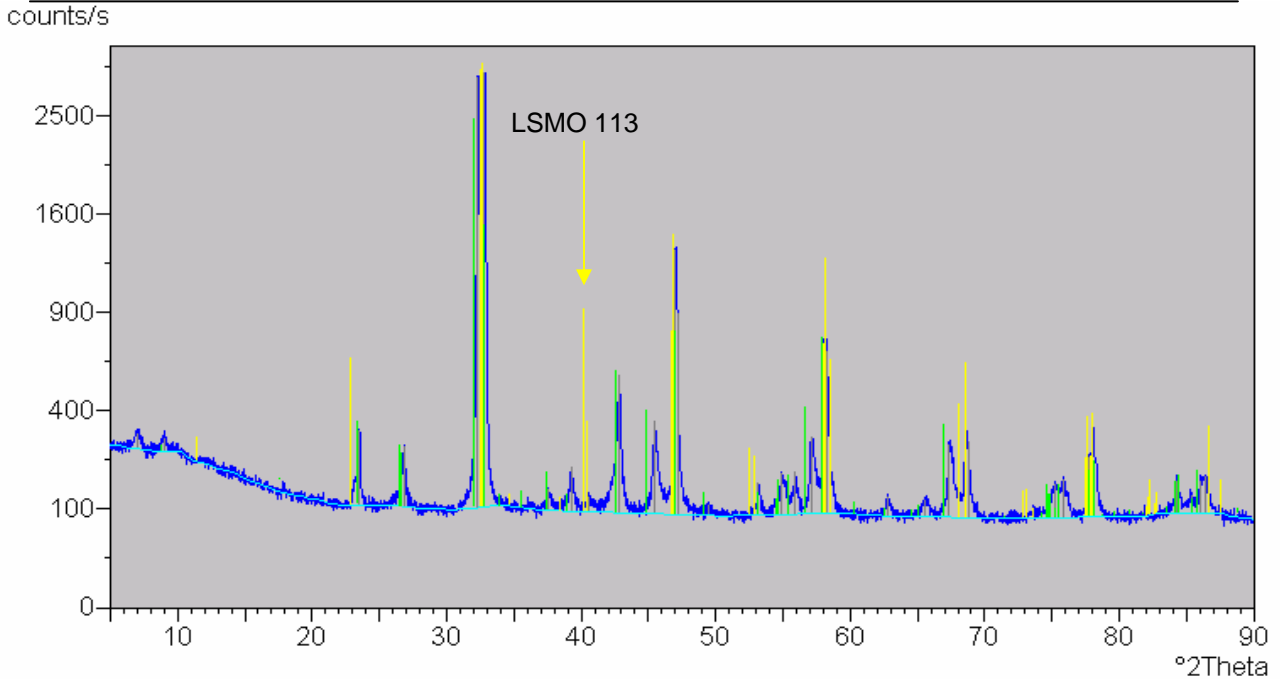


Figure 24: XRD of sintered sample with reference spectra of LSMO 327 (green) and 113 (yellow).

The experimental spectrum shows a close resemblance to the reference spectrum of  $\text{La}_{2.0}\text{Sr}_{1.0}\text{Mn}_2\text{O}_7$  and the sintered rod has the desired LSMO 327 phase. A minor peak at  $2\theta = 40.5^\circ$  however can only be ascribed to the LSMO 113 phase and indicates the presence of a second minor phase. The formation of the perovskite  $(\text{La,Sr})\text{MnO}_3$  as a parasitic phase seems to be a general problem as was also mentioned by K. Ruck et al<sup>30</sup>.

#### *Single Crystal Growth*

The sintered rod was used for single crystal growth in the optical furnace. The sample was rotated faster (30 rpm vs 20 rpm with the second sample) to narrow the temperature distribution and to homogenize the concentration within the zone.

After growth the sample was cut with a diamond saw to image the crosssection of the sample. The sample possessed two main grain boundaries that run through the whole length of the sample. In the crosssection one could see that the sample had formed a surface rim around the core (figure 25).

The sample possessed millimeter sized single

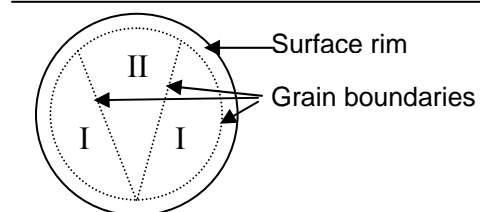


Figure 25: The crosssection of the sample exhibited several grain boundaries

crystals. A piece of the sample was cleaved along one of the grain boundaries and mounted in a sample holder together with the cross-section. Both were imaged with polarized optical microscopy, SEM and EPMA.

### *Polarized Microscopy*

In figure 26 the cross-section is shown as viewed by polarized microscopy (crossed polarizers, 50x). The cross-section exhibits various domains. These domains may differ in the orientation of the c-axis and represent different crystalline domains. The domains can however also differ in the orientation of the spins and give rise to different colors in polarized microscopy. The cross-section clearly exhibits a second phase in the rim of the sample, as the colors are very different from the matrix. The cross-section was analyzed with SEM and EPMA to image composition differences in the sample. The results of the SEM are not shown here as they are equivalent to the results obtained with the EPMA.

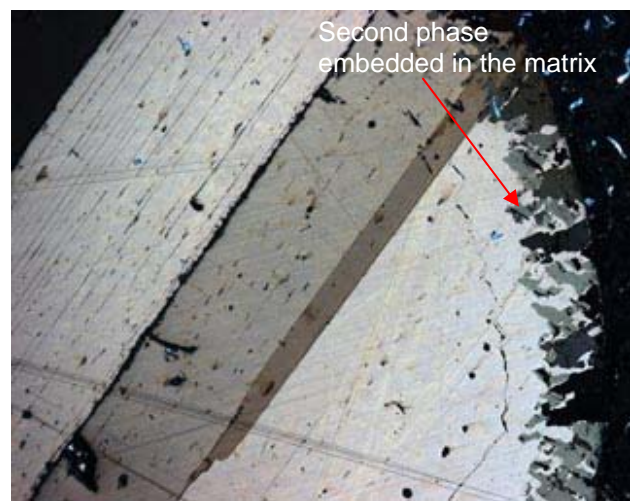


Figure 26: Cross-section viewed with crossed polarizers. Various domains and a second phase are visible.

### *Electron Probe MicroAnalysis*

In figure 27a (13.0 kV, 50x) the cross-section is imaged with EPMA. Three different features can be observed in the cross-section. The first feature is the presence of a second phase embedded in the matrix, in the surface rim of the sample.

Composition differences were also found in the core of the sample, though not as profound as in the surface rim.

The composition differences were present in two different forms. The first form was primarily present in region I (see single crystal growth) and was a wave-like stripe forming a complex pattern.

The second form was a regularly spaced straight-stripe pattern and was found in region II.

In figure 27b (20.0 kV, 300x) a detail of the wave-like stripe is shown. One can see that the stripes are regularly spaced and within the stripe a concentration-gradient is present. It is not clear what the driving force is for the formation of this pattern.

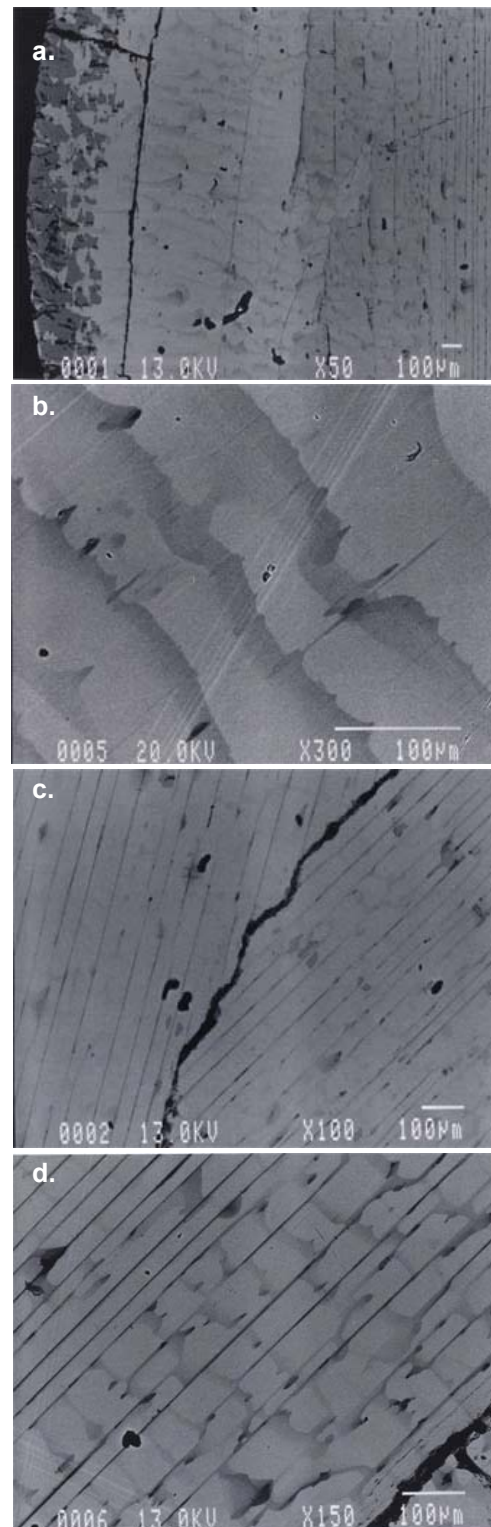
In figure 27c (13.0 kV, 100x) the straight-stripe pattern is shown. One can clearly see two different domains with different orientations which are separated by a grain boundary.

At first it was thought that the wave-like and straight stripes do not coexist and the presence of one pattern excluded the presence of the other one. This was contradicted by figure 27d (13.0 kV, 150x) in which one can see that the wave-like pattern intersects the straight-stripe pattern.

In figure 27e (20.0 kV, 5000x) a close-up of a stripe is shown. One can clearly see a concentration-gradient. The stripes are approximately 1  $\mu\text{m}$  in width. It is not clear why this phase segregation takes place.

The composition of the sample was determined using a cross-section and crystal surface piece of the sample.

The results are summarized in table 4.



The compositions measured in the matrix in the longitudinal and transversal sections of the rod show a rather different La/Sr ratio. The composition of the transversal section is close to the desired composition, the cross-section however has a too low La:Sr ratio.

The composition was also measured in the stripes, waves and in the rim in the cross-section of the sample. The stripes and waves have a too low La:Sr ratio. The rim has a too high La:Sr ratio of 1:1 versus the desired 1:1.5 ratio. This second phase has the perovskite LSMO 113 structure.

The formation of the perovskite (La,Sr)MnO<sub>3</sub> in the rim of the sample was also mentioned by M. Velázquez<sup>31</sup>. They found crystallites of the perovskite phase with x~0.45 in the periphery all along the as-grown material. They found that the lower the growth rate, the higher the perovskite volume fraction resulting from decomposition.

The composition was also measured in an area of 300x300 μm in the matrix with waves or stripes. The average composition shows that the La:Sr ratio in matrix was a too low. The Strontium concentration is too high compared to the Lanthanum and Manganese content and might be due to insufficient drying of the Lanthanum and evaporation of Manganese. Brownish material deposition on the quartz tube supports the latter argument. M. Velázquez also found a brownish material deposition on the tube and shafts and analyzed the chemical composition. EDX analysis revealed the presence of Mn, O and Sr (alkaline earths?). They found that the Mn volatilization is higher at lower growth rates, since volatilization is mainly a function of temperature and time.

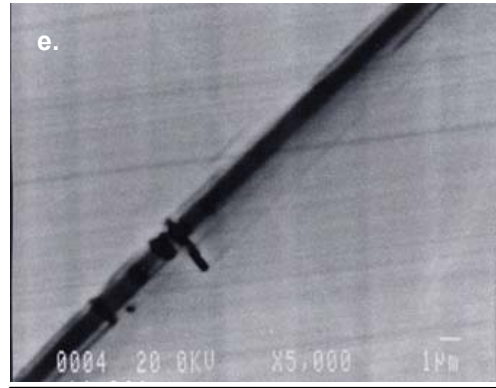


Figure 27a-e: different features imaged with EPMA

Table 4: Composition analysis carried out with EPMA on different features of the sample.

	<b>La</b>	<b>Sr</b>	<b>Mn</b>	<b>O</b>	<b>La+Sr</b>
Matrix transversal section	1.19	2.11	2.00	6.60	3.30
Matrix longitudinal section	1.15	1.83	2.00	5.74	2.98
Stripes	0.71	2.62	2.00	5.61	3.33
Waves	1.03	2.23	2.00	5.91	3.26
Rim	0.96	0.92	2.00	4.86	1.88
Averaged (300x300μm)	1.12	1.85	2.00	5.45	2.97

### Laue Diffraction

A thin piece of crystal at the end of the rod was used to take a Laue picture of the sample (25 kV, 40 mA, 5 min) and is shown in figure 28. The polychromatic beam was parallel to the c-axis of the crystal.

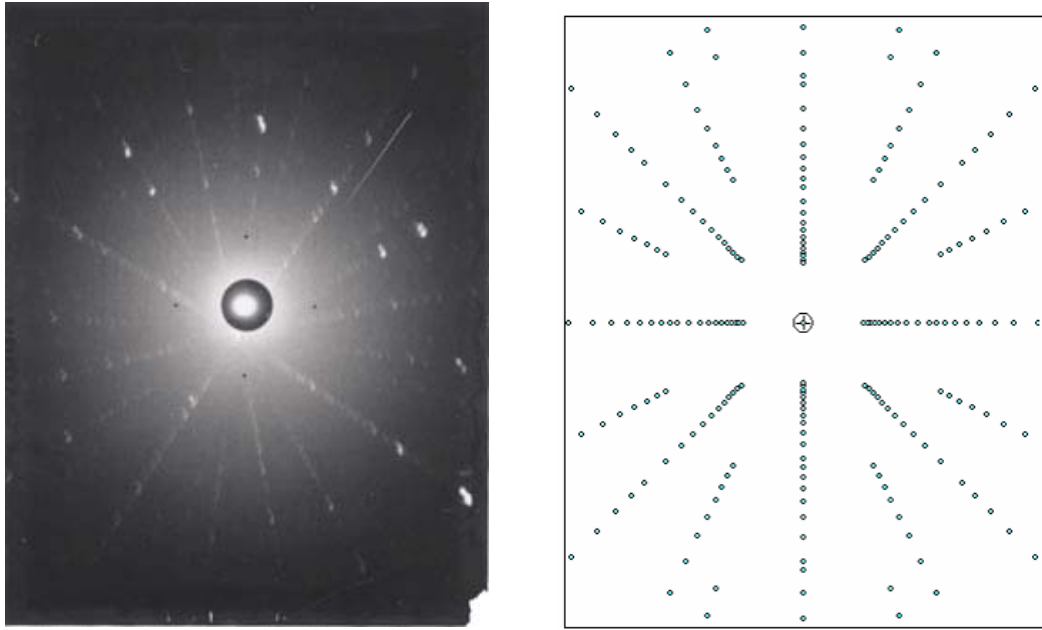


Figure 28: experimental and reference Laue pictures of  $\text{La}_{1.2}\text{Sr}_{1.8}\text{Mn}_2\text{O}_7$

The picture shows a close resemblance to the reference spectrum of  $\text{La}_{1.2}\text{Sr}_{1.8}\text{Mn}_2\text{O}_7$ , although in the experimental picture more orders can be seen. One can conclude the sample has the correct phase. The points are however built up from multiple points, indicating the measured sample is not a single crystal, but rather composed of crystal domains which are twisted with respect to each other.

The points in the Laue picture are not point-like, but are rather elongated, indicating a deviation from the perfect crystal structure. Several brighter spots are also present, as was also found for the second sample and it is not clear what the reason is for this feature.

### SQUID

The magnetization as a function of temperature was measured in a field of 50 Gauss in two modes; Zero-Field Cooling and Field cooling. The two M-T diagrams are shown in figure 30.

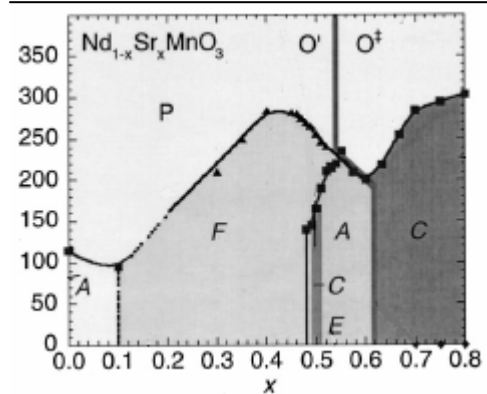


Figure 29: Phase diagram of  $\text{Nd}_{1-x}\text{Sr}_x\text{MnO}_3$  crystals. The letters refer to Paramagnetic (P), Ferromagnetic (F), A-type Antiferromagnetic (A), CE-type ferromagnetic (CE) and C-type Antiferromagnetic spin ordering

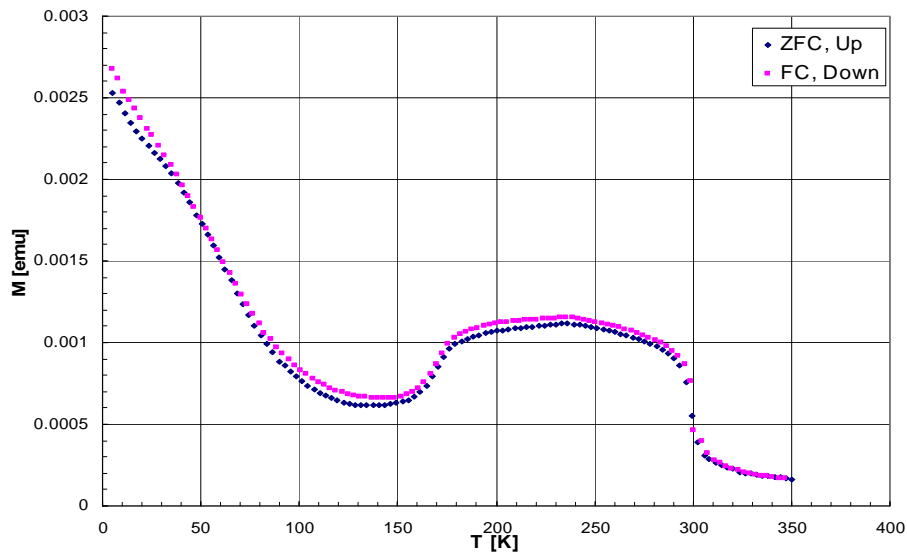


Fig 30: Magnetization as a function of temperature

The M-T diagram exhibits a plateau between  $T = 175\text{--}300\text{ K}$  and corresponds to a ferromagnetic state. When selecting a crystal to measure with the SQUID, the surface rim sticks to a magnet, also indicating its ferromagnetic state at room temperature. This is not in accordance with the LSMO 327 phase. Composition analysis showed that the rim contains the LSMO 113 phase. In the phase diagram<sup>32</sup> (figure 29) of a similar structure  $\text{Nd}_{1-x}\text{Sr}_x\text{MnO}_3$ , one can see a Paramagnetic-Ferromagnetic-Antiferromagnetic transition for  $x \approx 0.5$ . This might explain the magnetization curve in our sample. In the M-T diagram a Paramagnetic-Ferromagnetic transition occurs at  $T = 300\text{ K}$ .

The decreasing magnetization at  $T = 170\text{ K}$  is probably due to a reorientation of the spins towards an Antiferromagnetic state. It is not clear what type the AFM state is. The reorientation of the spins to an AFM state is supported by the Magnetization vs Field diagram (Appendix figure 2). The sample has zero spontaneous magnetization in  $T = 135\text{ K}$ , a property of the antiferromagnetic state.

In the appendix figure 1 a M-T diagram is shown in which the features of the LSMO 113 phase are shown. One can clearly see the PM-FM-AFM transitions without the contributions from the LSMO 327 phase.

For  $T < 100\text{ K}$  the diagram shows a resemblance to the diagram of the LSMO 327 phase, although the presence of the LSMO 113 phase influences the magnetization.

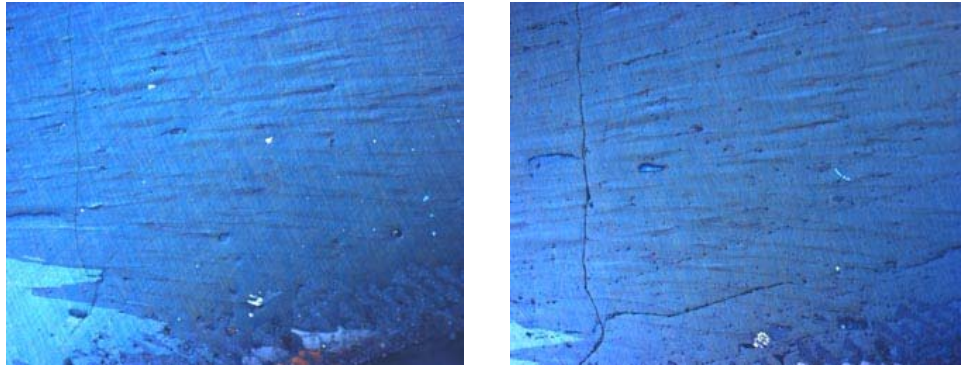
The magnetization vs the field for  $T = 5\text{ K}$  shows that the sample has a non-zero magnetization at zero field, indicating a ferromagnetic field. This corresponds to the LSMO 327 phase which is ferromagnetic at low temperatures.

Although these are the main features of the diagram, the diagram is still not completely understood. The sample is a two-phase system in which one of the phases contains composition differences as well, making the diagram complicated and hard to understand as the phases probably couple to each other.

### *Annealing*

To determine the effect of annealing on the inhomogeneous composition pattern a crystal piece was imaged with polarized microscopy before and after annealing (figure 31). The sample was cleaved along one of the two grain boundaries and the region with the straight stripes was imaged. In order to compare the effect of annealing the sample was grinded and polished in a brass sample holder and imaged with polarized microscope and thereafter annealed in air in 1400 °C for 100 h and taken out at 1300 °C.

---



---

Figure 31: Polarized microscopy pictures of the crystal surface before (left) and after (right) annealing (1400 °C 100 h, quenched in air)

As one can see the annealing did not have any effect. Thus either the annealing was not sufficient or the composition segregation is an energy favored configuration in the sample.

## Sample 4

### *X-Ray Diffraction*

In figure 32 the XRD taken after the first sintering (1400°C 32 h) is shown together with reference spectra of  $\text{La}_{2.0}\text{Sr}_{1.0}\text{Mn}_2\text{O}_7$  (green) and  $\text{La}_{0.65}\text{Sr}_{0.35}\text{MnO}_3$  (yellow).

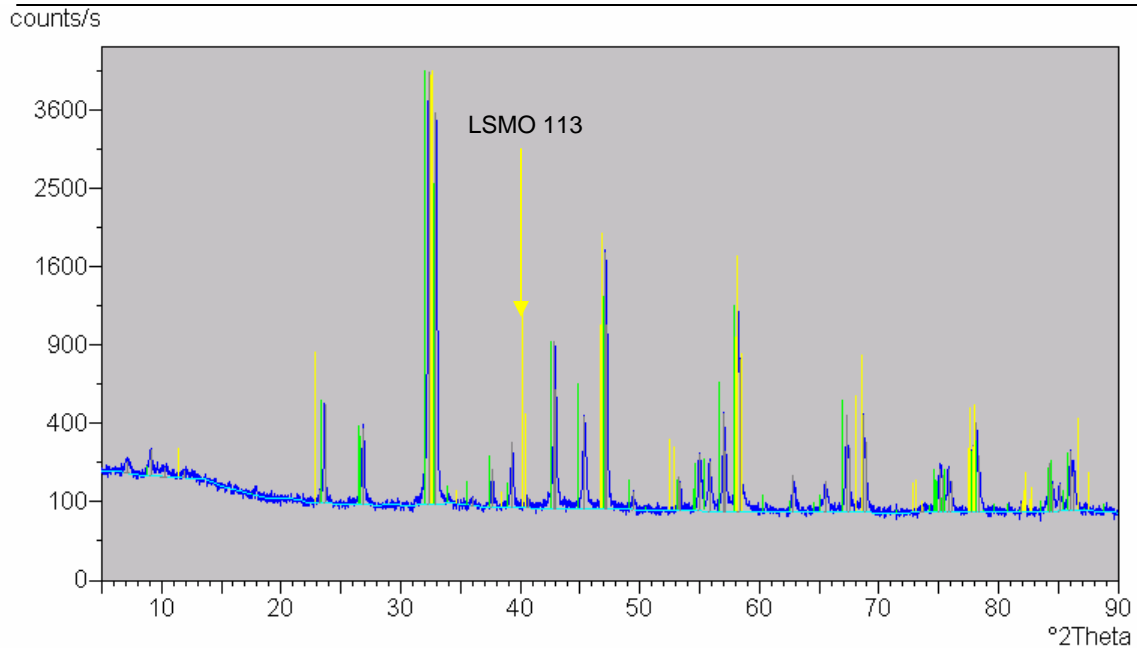


Figure 32: XRD of the sample after the first sintering (1400°C 32h). The reference spectra of LSMO 327 (green) and 113 (yellow) are also shown. The minor peak at  $2\theta = 40.5^\circ$  (yellow arrow) indicated the presence of the LSMO 113 phase.

As before a peak at  $2\theta = 40.5^\circ$  (yellow arrow) indicated the presence of a minor fraction of the LSMO 113 phase in the sample.

The sample was after this session sintered for the second time (1400 °C 24 h), pressed into a rod and sintered at 1450°C for 24 h and 1500°C for 2 h. The rod was used in the optical furnace single crystal growth.

### *Single Crystal growth*

The melting of the sample was not uniform in the beginning and stabilization of the floating zone was complicated by this. This was probably due to the lamps, since one of the halogen lamps broke after 37 mm growth.

The cross-section of the sample looked more uniform compared to the previous sample, although many grain boundaries were present. With the microscope one could again see a surface rim around the sample, probably indicating the presence of a second phase. The sample possessed smaller sized single crystals compared to the previous samples.

A cross-section of the sample at the beginning of the growth was cut with the diamond saw and imaged with polarized microscopy and SEM.

A thin crystal piece was selected to perform Laue Diffraction and SQUID was carried out on a crystal piece from the core and from the rim of the sample.

### *Polarized Microscopy*

In figure 33a the crosssection is shown as viewed with polarized microscopy (87 °, 50x). One can see several domains which are smaller compared to sample 3 (figure 16). This is due to the fact that the growth of the crystal just began.

Composition differences could only be seen clearly in the rim. A close-up of the rim is shown in figure 23b (87°, 200x). The spots are embedded in the matrix and are smaller compared to sample 3.

The sample was analyzed with SEM to image composition differences more clearly.

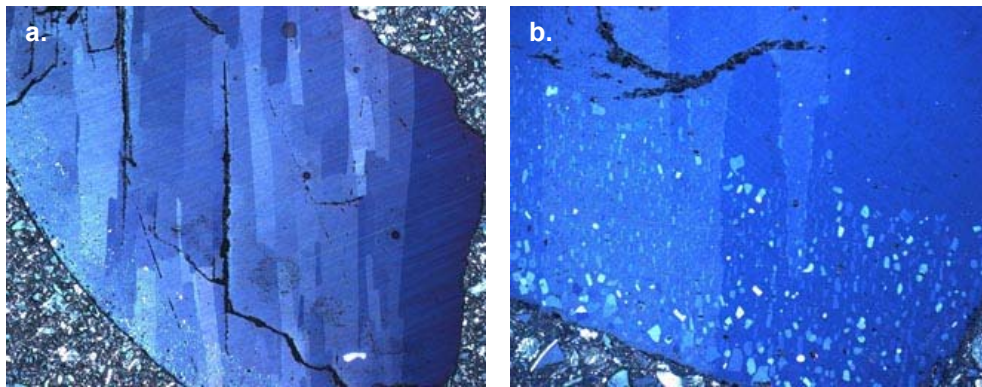


Figure 33 a: Crosssection as viewed polarized microscopy (50x), showing different domains in the sample.  
Figure 33 b: Rim as viewed polarized microscopy (200x) showing composition differences in the rim.

### *Scanning Electron Microscopy*

The crosssection was analyzed in Backscattered electron mode to image the composition differences in the sample. In figure 34 a-d the SEM images taken with different magnifications are shown.

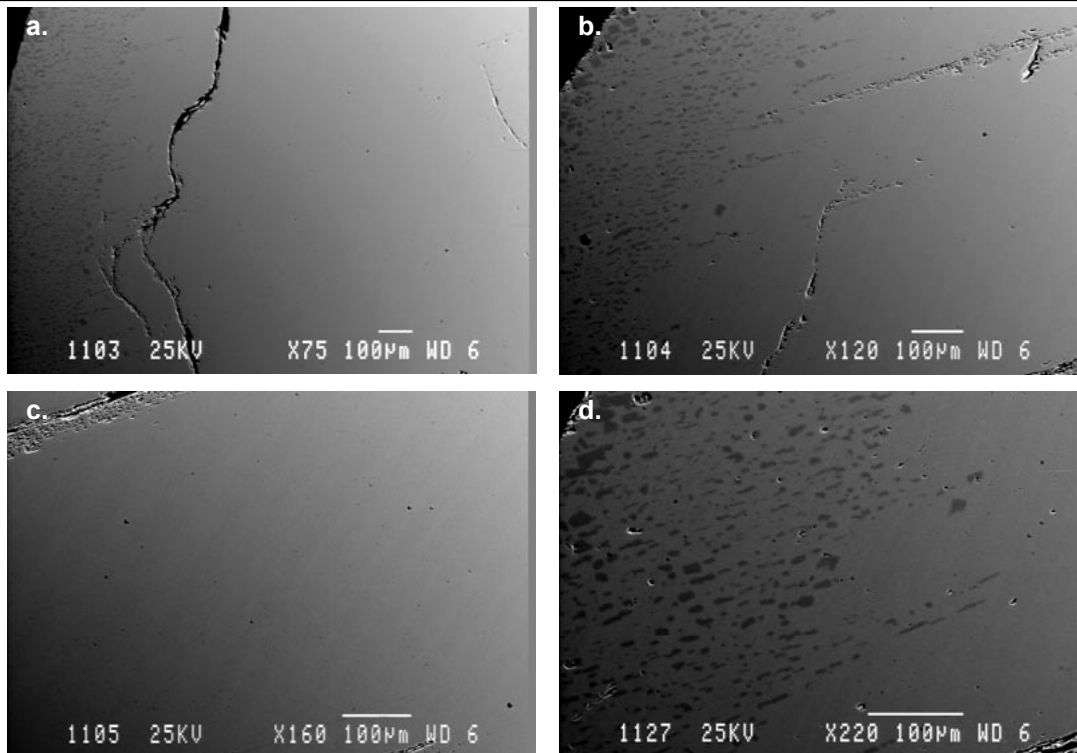


Figure 34 a-d: Crosssection viewed with SEM with different magnifications; a) 75x b) 120x c) 160x showing the matrix is free of composition differences d) 220x showing composition differences in the rim.

In figure 34a half of the embedded crosssection is imaged and composition differences are only observed in the rim of the sample. In figure 34b and 34d one can see the spots more clearly. In figure 34 c the matrix of the sample is imaged and composition differences could not be observed. Although one can see vague stripes in the matrix caused by the grinding and polishing process. At larger magnifications no composition differences could be observed either.

Faster growth rate thus tends to make the sample homogeneous in composition, although composition differences in the rim remain. Unfortunately composition analysis could not be performed to analyze the chemical composition.

The volume fraction of the perovskite phase also decreased with increasing growth rate, as was claimed before by M. Velázquez.

The domains that were visible with polarized microscopy could not be observed with SEM, thus indicating the domains are not due to composition differences in the sample.

In the Discussion a mechanism for the formation of an inhomogeneous composition pattern will be discussed.

### *Laue Diffraction*

In figure 35 the Laue Picture taken from a thin single crystal is shown. The picture shows a resemblance to the generated Laue pattern. The sample has the correct crystal structure.

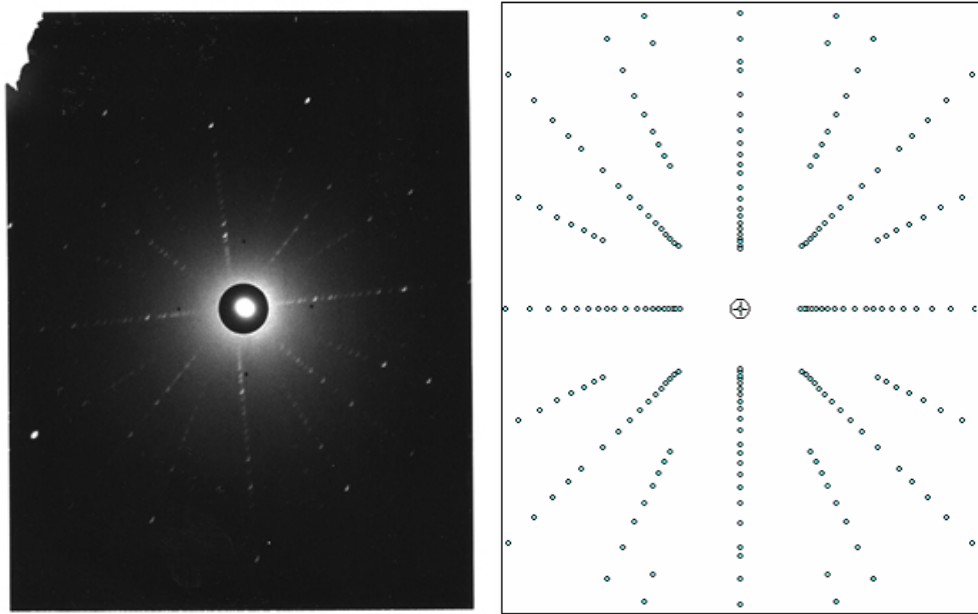


Figure 35: experimental and reference Laue pictures of  $\text{La}_{1.2}\text{Sr}_{1.8}\text{Mn}_2\text{O}_7$

The points in the Laue picture are a bit elongated, indicating a deviation from the perfect crystal structure. Comparing the Laue picture with the Laue pictures of sample 2 and 3 one can however conclude that this crystal piece is of a better quality as the spots are more point-like.

## SQUID

A small crystal piece from the core was used to measure the magnetization as a function of the temperature ( $T= 5\text{K}-400\text{K}$ ) to determine the Curie temperature. The M-T diagram is shown in figure 36.

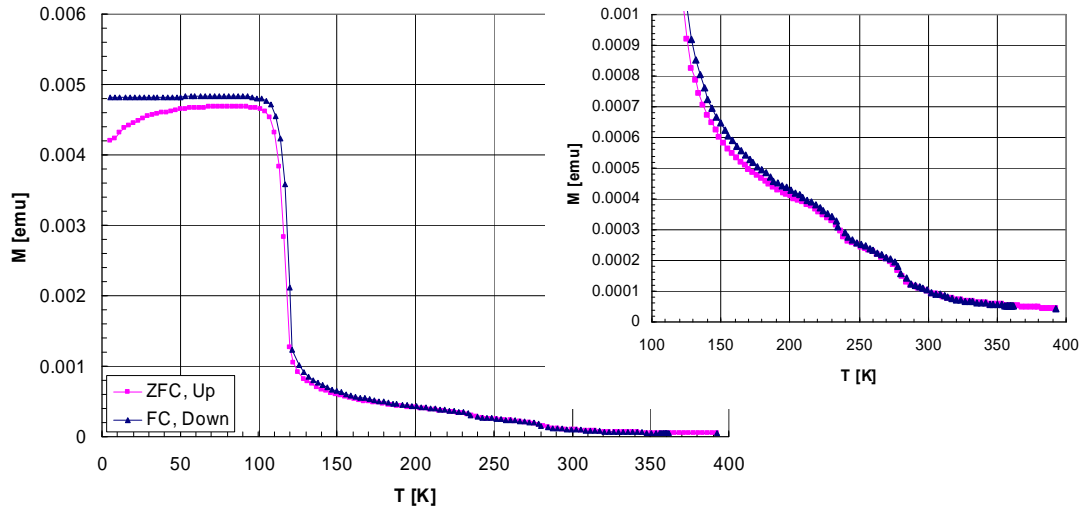


Fig 36: Magnetization as a function of temperature,  $T_c=120$  K. Inset shows step-like behavior for  $T>230\text{K}$ .

The diagram is recorded with Zero-Field Cooling (ZFC) and Field-Cooling with a magnetic field of 50 Gauss. The diagram looks similar to the diagram recorded for the second sample with  $T_c= 120$  K. The paramagnetic-ferromagnetic transition is sharp and gives promising results.

The inset shows a close-up of the step-like behavior for  $T>230$  K and was also found in the second sample.

## 4. Discussion

### *Inhomogeneous composition pattern*

The phase diagram of the ternary LSMO system is shown in figure 37 and was published by K. Ruck<sup>30</sup>. Samples with different compositions marked in the phase diagram were prepared by solid-state reactions of appropriate amounts of  $\text{La}_2\text{O}_3$ ,  $\text{SrCO}_3$  and  $\text{Mn}_2\text{O}_3$  and heated 1 week at 1350 °C. The phase diagram is a graphic representation of the phases that were obtained. Ruck prepared samples with  $n=2$  (LSMO 327),  $n=3$  (three-layer compounds LSMO 4310) and  $n=\infty$  (LSMO 113).

The results they obtained for the bilayer (red line) will be discussed to get a better understanding of the system.

Ruck obtained pure-phase compounds for LSMO 327 for  $0.4 < x < 0.7$  indicated by the circles. For compositions between  $\text{La}_{1.4}\text{Sr}_{1.6}\text{Mn}_2\text{O}_7$  and  $\text{La}_{2.0}\text{Sr}_{1.0}\text{Mn}_2\text{O}_7$  ( $0 < x < 0.3$ ) a three phase system was obtained consisting of  $\text{La}_2\text{O}_3$ -bilayer-perovskite, indicated with the crosses. For  $0.325 < x < 0.375$  traces of perovskite already appeared (triangle).

The authors also tried to prepare three-layer compounds, but this member of the Rudlessden-Popper series appeared not to be stable for this preparation procedure and the system always formed the bilayer and perovskite phases.

The LSMO 113 phase has a large composition range and is indicated by the grey area.

To explain the formation of a stripe pattern in the samples, a mechanism will be proposed.

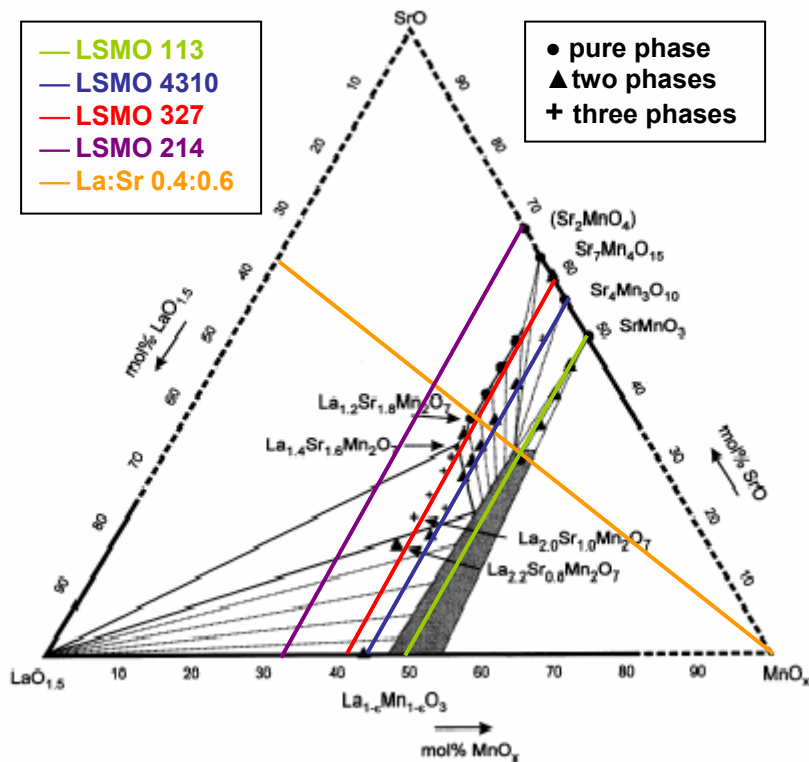


Figure 37: phase diagram of the ternary LSMO system. Experimental points were measured by Ruck. The colored lines represent LSMO phases in which the La:Sr ratio can vary. The orange line represents the La:Sr ratio which is used in this experiment.

Two different composition inhomogeneities were found in the sample: the formation of the LSMO 113 phase in the rim and the formation of stripes with different La:Sr ratios from the matrix. The first inhomogeneity can be studied using the orange line, in which the La:Sr ratio is fixed, but the manganese content varies, resulting in different LSMO phases. The different LSMO phases are indicated with colored lines.

In figure 38 a schematic phase diagram and mechanism for the formation of the LSMO 113 as a foreign phase is proposed. An experimental phase diagram for the formation of other members of the Ruddlesden-Popper series was not known to the authors. In order to explain the formation of the LSMO 113 phase in the rim of the sample as a function of temperature, a schematic phase diagram and mechanism is proposed. This phase diagram runs along the orange line in the ternary phase diagram.

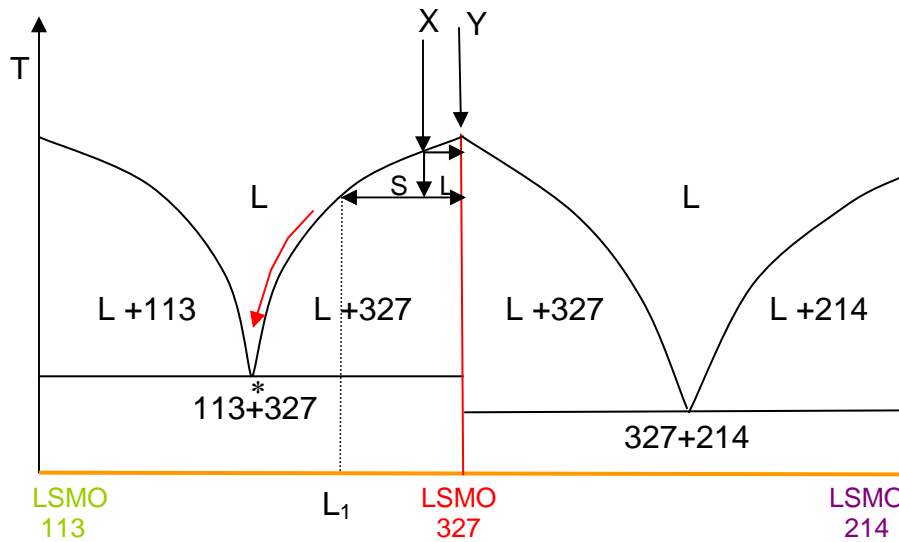


Figure 38: Proposed phase diagram of the LSMO system in which only the formation of other LSMO phases is taken into account. The variation of the La:Sr is not taken into account here.

Assuming the solidification line of the LSMO 327 has the right (La,Sr):Mn ratio, cooling down a sample with composition Y will result in the formation of the desired phase in the desired composition.

If however a sample with a deviating composition X is cooled down in the L+327 region, part of the sample will crystallize in the desired 327 phase.

The solid LSMO 327 phase is balanced by a portion of liquid with composition  $L_1$ . This is shown in figure 38. The Lever rule states that the fraction left of the starting composition is solid and the right fraction is liquid. Thus with decreasing temperature this fraction of liquid is reduced. At the eutectic temperature (\*) the remaining liquid will solidify into the LSMO 113 and 327 phase by eutectic reaction.

A small composition difference between the solidification line and the starting composition line can thus already cause the formation of a second phase. The same situation is drawn for the 327 and 214 phases.

This mechanism is supported by the fact that the core consists of the LSMO 327 phase and only the rim has the LSMO 113 phase embedded in the matrix.

The solidification process starts in the core of the sample as the temperature is lower there than close to the surface of the rod. The core of the sample will solidify in the LSMO 327 phase and is balanced by a portion of liquid with another composition. A fraction of this liquid eventually solidifies at the surface of the sample and if it reaches the eutectic point it will solidify into the LSMO 113 and 327 phases.

To understand the inhomogeneous stripe patterns found for samples 2 and 3, a schematic phase diagram is proposed in figure 39. The phase diagram is drawn for the LSMO 327 phase (red line) in which the Mn-content stays constant and the La:Sr ratio varies.

A sample with starting composition  $X$  is cooled down in the  $L+\alpha$  phase. At  $T_0$  the sample is still totally liquid with starting composition  $C_3$ . Cooling down the sample to  $T_1$  will result in solidification of the sample with composition  $C_1$  and this solid is balanced by a liquid with composition  $L_1$ . Since in the floating zone technique a temperature gradient is present, the sample can also solidify at  $T_2$  with composition  $C_2$ . This solid is again balanced by a portion of liquid with composition  $L_2$ . The liquid will eventually reach the point with concentration  $C_3$ .

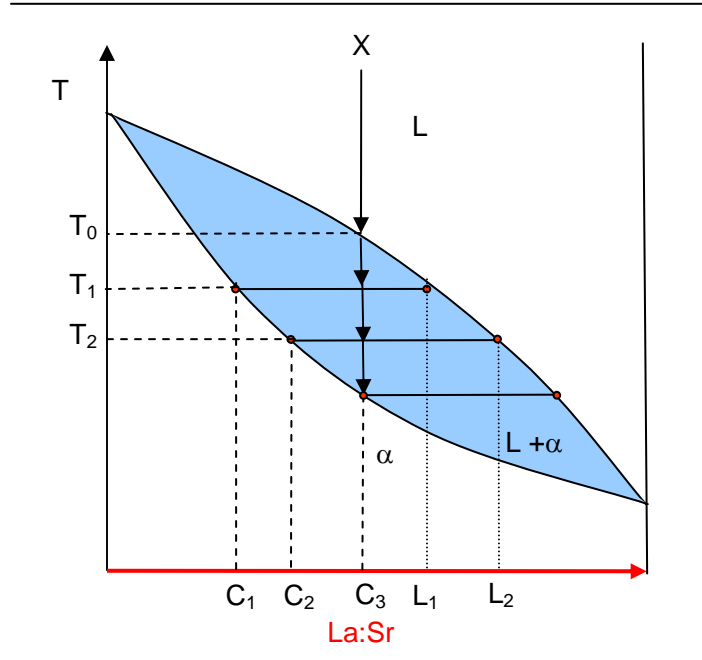


Figure 39: proposed schematic phase diagram to explain the formation of a stripe-pattern found in sample 2 and 3.

The formation of a stripe pattern can be explained in the following way (figure 40): the sample tends to crystallize along the  $ab$ -planes, as the  $c$ -axis is very long, forming plate-like domains. The growth direction is therefore parallel to the  $ab$ -planes. As a temperature gradient is present in the floating zone, part of the sample will solidify at  $T_1$  with composition  $C_1$  and the part of the sample which has temperature  $T_2$  will solidify with composition  $C_2$ , these processes takes place at the same time. In the samples that were obtained, the composition differences were found to be plate-like, parallel to the growth direction.

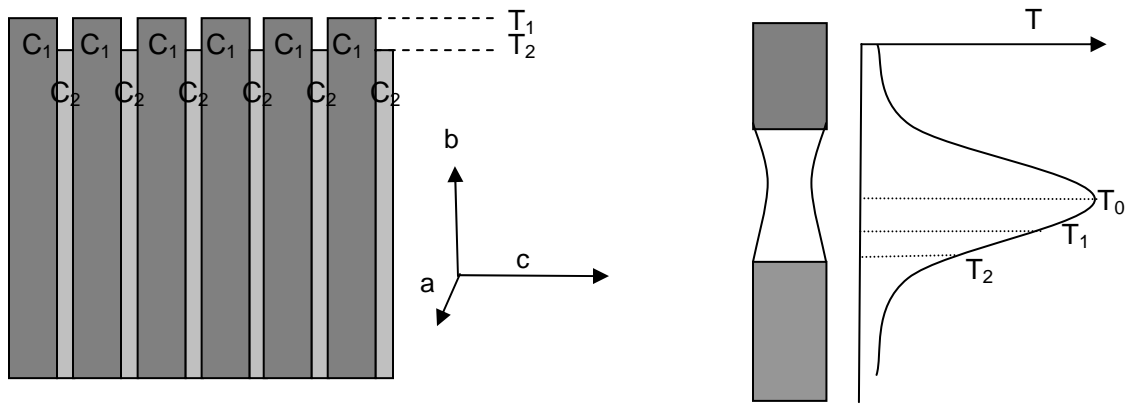


Figure 40: the formation of plate-like domains which differ in composition due to the presence of a temperature gradient (right). The temperature gradient present in the floating zone (left)

Another possibility for the formation of a stripe pattern can be explained using the phase diagram in figure 39. Since the sample solidifies at  $T_1$  the solid with composition  $C_1$  will be balanced by a liquid with composition  $L_1$ . This liquid will be present at the solidification interface. While the zone is moved along the sample, this liquid will solidify at a lower  $T$  than  $T_1$  resulting in a different composition than  $C_1$ . As was explained earlier, the crystal tends to crystallize along the  $ab$ -planes resulting in plate-like domains. The liquid balancing the solid will crystallize between these plates at a lower temperature than  $T_1$  resulting in a stripe-like pattern.

To summarize: two possible mechanisms were suggested to explain the stripe-like pattern. The first mechanism explains the formation of a stripe-like pattern in the light of the temperature-gradient present in the floating zone. The sample will crystallize in plate-like domains, and crystallization in different compositions takes place due to the temperature-gradient.

The other mechanism suggests that the formation of an inhomogeneous composition pattern is due to the fact that the solidifying crystal is balanced by a liquid with another composition. This liquid is close to the solidifying interface and will crystallize into another composition, resulting in a stripe-like pattern.

It should be stressed that the mechanisms proposed here are suggestions and no experimental phase diagram of the system was known to the author to support the proposed mechanisms.

## 5. Conclusion

Millimeter-sized Single crystals of the double layered manganite  $\text{La}_{1.2}\text{Sr}_{1.8}\text{Mn}_2\text{O}_7$  were grown using the Traveling Floating Zone Technique. Analysis of the longitudinal and transverse sections with Electron Microscopy showed the presence of composition inhomogeneities in the sample. In the rim of the sample the LSMO 113 phase was embedded in the matrix in a spot-like pattern. A second composition inhomogeneity was found in the matrix in a stripe-like pattern. The stripes had the same LSMO 327 structure as the matrix, but differed in the La:Sr ratio.

Two mechanisms were proposed to understand the formation of this concentration inhomogeneity using proposed phase diagrams.

When the growth rate was increased from 10 mm/h to 15 mm/h it was found that the matrix of the sample did not show composition differences. The volume fraction of the foreign perovskite phase in the rim was decreased by the faster growth.

## Appendix A

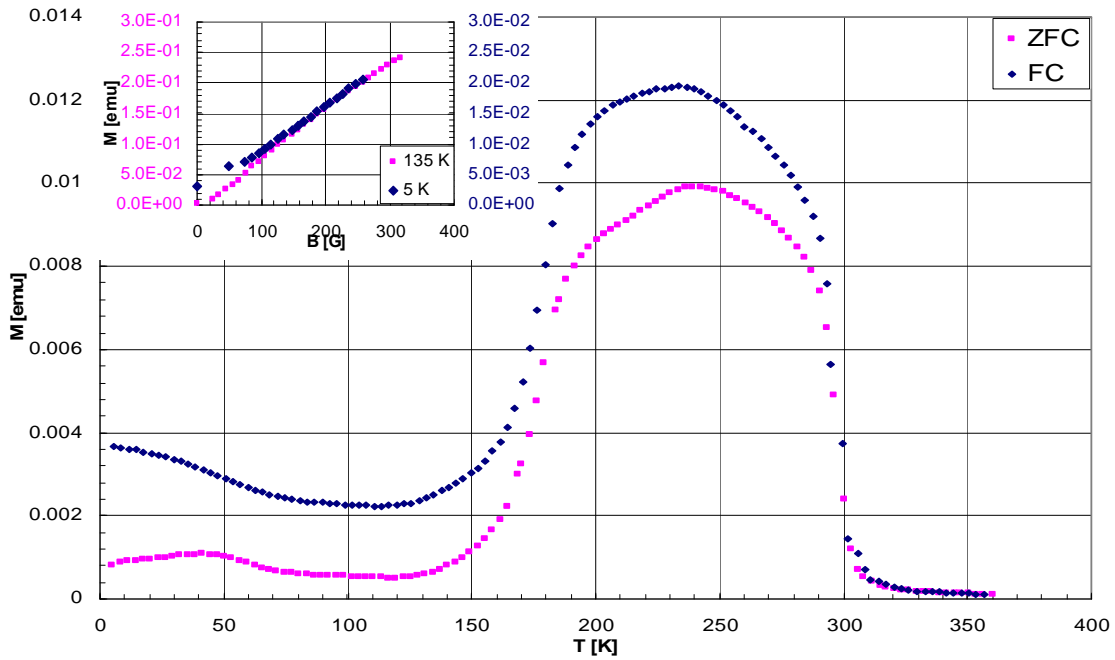


Figure A1: Magnetization vs Temperature for sample 3. The Paramagnetic-Ferromagnetic-Antiferromagnetic transitions are a feature of the LSMO 113 phase,  $x \approx 0.5$ . The inset shows the magnetization as a function of the field, the linear behavior and extrapolation to  $M=0$  indicates that the transition is an antiferromagnetic one (pink). When the magnetization  $\neq 0$  at  $H=0$  than the system has a spontaneous magnetization and is ferromagnetic. This is a feature of the LSMO 327 phase which is FM at low temperatures.

## References

---

- <sup>1</sup> D.S Dessau, Y.D Chuang, A. Gromko et al., Journal of Electron Spectroscopy and related phenomena **117-118**, 265-276 (2001)
- <sup>2</sup> J.F Mitchell, D.N Argyriou, J.D Jorgensen, Physical Review B **55** number 1, 63 (1 January 1997)
- <sup>3</sup> M.B. Salomon, M. Jaime, Reviews of Modern physics **73**, 583 (July 2001)
- <sup>4</sup> K.Hirota, S.Ishihara, H. Fujioka et.al, Phys.Rev.B **65**, 064414 (2002)
- <sup>5</sup> Y.-D Chuang, A.D Gromko, D.S Dessau et al., Science **292**, 1509 (25 May 2001)
- <sup>6</sup> D.S Dessau, Z.-X Shen, Direct Electronic Structure Measurements of the Colossal Magnetoresistive Oxides, 1998
- <sup>7</sup> B.J Campbell, R. Osborn, D.N Argyriou et al., arXiv:cond-mat?0106477 v2 9 juli 2001
- <sup>8</sup> T. Saitoh, D.S Dessau, Y. Moritomo et al., Physical Review B **62** number 2, 1039 (1 July 2000)
- <sup>9</sup> D.S Dessau, T. Saitoh, C.-H Park et al., Physical Review Letters **81** number 1, 192 (6 July 1998)
- <sup>10</sup> D.S Dessau, T. Saitoh, C.-H Park et al., Journal of Superconductivity **12** number 1, 273 (1999)
- <sup>11</sup> <http://num.web.psi.ch/reports/2003/lms/ms-10.pdf>
- <sup>12</sup> <http://www.tulane.edu/~sanelson/eens211/x-ray.htm>
- <sup>13</sup> <http://www.mrl.ucsb.edu/mrl/centralfacilities/xray/xray-basics/Xray-basics.html#x1>
- <sup>14</sup> [http://www.matter.org.uk/diffraction/x-ray/powder\\_method.htm](http://www.matter.org.uk/diffraction/x-ray/powder_method.htm)
- <sup>15</sup> <http://www2.umist.ac.uk/material/research/intmic/schools/schools/laue/sample.htm>
- <sup>16</sup> <http://journals.iucr.org/iucr-op/comm/cteach/pamphlets/2/node7.html#SECTION00061000000000000000>
- <sup>17</sup> [http://www.matter.org.uk/diffraction/x-ray/laue\\_method.htm#](http://www.matter.org.uk/diffraction/x-ray/laue_method.htm#)
- <sup>18</sup> <http://www.olympusmicro.com/primer/techniques/polarized/polarizedintro.html>
- <sup>19</sup> <http://www.nikon-instruments.jp/eng/tech/2-1-3-1.aspx>
- <sup>20</sup> <http://hyperphysics.phy-astr.gsu.edu/hbase/solids/squid.html#c3>
- <sup>21</sup> <http://www.physics.carleton.ca/courses/75.364/mp-2html/node23.html>
- <sup>22</sup> <http://www.adpc.purdue.edu/PhysFac/rem/rs/sem.htm>
- <sup>23</sup> <http://www.unl.edu/CMRACfem/semoptic.htm>
- <sup>24</sup> <http://www.mse.iastate.edu/microscopy/source.html>
- <sup>25</sup> <http://www.unl.edu/CMRACfem/interact.htm>
- <sup>26</sup> <http://epmlab.uoregon.edu/epmatext.htm>
- <sup>27</sup> <http://jan.ucc.nau.edu/%7Ewittke/Microprobe/ProbeIntro-EMP.html>
- <sup>28</sup> S.H Chun, Y. Lyanda-Geller, M.B Salomon, arXiv-cond-mat/0007249v1 (14 juli 2000)
- <sup>29</sup> N.O Moreno, P.G Pagliuso, C. Rettori et al. Physica B **292**, 1-8 (2000)
- <sup>30</sup> K.Ruck, M. Sgraja, K. Grabbes et. Al, Journal of Alloys and Compounds **306**, 151-157 (2000)
- <sup>31</sup> M. Velázquez, C. Haut, B. Hennion et.al., Journal of Crystal growth **220**, 480-487 (2000)
- <sup>32</sup> M.B Salamon, M. Jaime, Reviews of modern Physics **73**, 583 (2001)